Chapter 12
The Role of the Earth's Rotation: Oscillations in Semi-bounded and Bounded Basins of Constant Depth

12.1 Motivation

In Chap. 7 of Volume I, the propagation of surface waves in a layer of a homogeneous fluid referred to an inertial frame was studied. It was shown that superposing the fields of two waves, with the same frequency propagating in opposite directions with the same amplitude can be combined to a standing wave. These standing waves appear as localized oscillations between fixed nodal lines of which the distance defines the semi-wave length with wave humps and wave troughs arising inbetween. Under frictionless conditions imaginary walls can be placed at any position parallel to the wave direction to confine a channel without physically violating any boundary conditions. Similarly, the locations of the nodal lines across the channel turned out to be the positions of standing waves where the longitudinal velocity component vanishes for all time so that vertical walls can equally be inserted at these positions without disturbing the solution. This then formally yields the surface wave solution for the unidirectional motion in a basin of rectangular form and constant depth, see Figs. 7.9 and 7.12 in Chap. 7 of Volume I. These standing wave solutions were subsequently generalized to two-dimensional oscillations in rectangular cells of constant depth in which non-vanishing horizontal velocity components are allowed within the cell that only persistently vanish at the four side walls, thus forming oscillations of true cellular structure (see Figs. 7.14 and 7.15 in Chap. 7 in Volume I). How does the structure of these waves change when the fluid is rotating?

In Chap. 11, a first analysis of the role of the influence of the rotation of the Earth was provided. It was shown that in constant depth basins the water motion in a stratified fluid layer can in the shallow water approximation be split into a vertical problem defining the barotropic and baroclinic components (due to stratification) and a horizontal problem. It is the latter which chiefly describes the role of the rotation of the Earth via the dispersion relation and the Coriolis-acceleration terms in the horizontal momentum equations. The stratification enters this dispersion relation through the eigenvalues of the vertical problem but a feed back of the rotation of the Earth to the vertical problem does not arise. Therefore, in the shallow water approximation the baroclinic mode structure is not influenced by the rotation of the Earth,

K. Hutter et al., *Physics of Lakes*, *Volume 2: Lakes as Oscillators*, Advances in Geophysical and Environmental Mechanics and Mathematics,
DOI 10.1007/978-3-642-19112-1_12,

whilst the horizontal problem is affected by the former.[1] We determined in Chap. 11 also the harmonic wave solution to the horizontal problem by using a plane wave ansatz for a wave propagating in the infinite horizontal plane. The corresponding waves have super inertial frequencies, are called Poincaré-(Sverdrup)-waves, and only have real frequency and real wavenumber in infinite space. Complex valued wavenumbers and frequencies will yield exponential growth or decay in space and time and then require bounded domains.

In this chapter, we focus attention on the role played by the rotation of the Earth in the horizontal problem. In other words, we address the question how the rotation of the Earth alters the solutions as constructed in Chap. 7 in Volume I and Chap. 11.

Whereas the theory has been developed by prominent mathematicians, of the 19th century and the first half of the 20th century (Kelvin, Poincaré, Sverdrup, Taylor, Helmholtz, Goldstein, Rossby...) the graphical interpretation of the results has chiefly been done by Mortimer [24–27].

12.2 Kelvin Waves

Consider a water layer of constant depth bounded at $y = 0$ by a vertical wall. We shall see later on that, alternatively, we may equivalently consider an infinitely long canal with vertical side walls parallel to the x-axis positioned at $y = 0$ and $y = B$. In the shallow water approximation, the governing equations of the free water motion are given by the layer averaged mass and momentum balances,

$$\left.\begin{aligned} &\frac{\partial \zeta}{\partial t} + \frac{\partial U}{\partial x} + \frac{\partial V}{\partial y} = 0, \\ &\frac{\partial U}{\partial t} - fV = -gh_{\text{bar}}\frac{\partial \zeta}{\partial x}, \\ &\frac{\partial V}{\partial t} + fU = -gh_{\text{bar}}\frac{\partial \zeta}{\partial y}, \end{aligned}\right\} (x, y, t) \in (-\infty, \infty) \cup [0, \infty) \cup \mathbb{R}^+, \tag{12.1}$$

in which $\boldsymbol{M} \hat{=} (U, V)$, ζ is the displacement of the free surface from the un-deformed surface at rest, and $h_{\text{bar}} = H$ is the constant water depth.

We have seen in Chap. 7 in Volume I that plane waves in a non-rotating infinitely long channel propagate parallel to the side walls and have vanishing transverse velocity ($V \equiv 0$) throughout the channel. It is, therefore, tempting to assume that also (12.1) possess such a solution. Therefore, we let

$$\left.\begin{aligned} &\zeta = \zeta_0 \Phi(y) \exp\left[i(kx - \omega t)\right], \\ &U = u_0 h_{\text{bar}} \Phi(y) \exp\left[i(kx - \omega t)\right] \\ &V \equiv 0, \end{aligned}\right\} (x, y, t) \in (-\infty, \infty) \cup [0, \infty) \cup \mathbb{R}^+, \tag{12.2}$$

[1] Recall that in formulations which are not based on the shallow water approximation the coupling can be shown to be two-sided.

in which k is the wavenumber and ω the circular frequency. In (12.2), we assumed that ζ and U propagate harmonically into the positive x-direction with phase speed $c_{\mathrm{ph}} = \omega/k$. Both, ζ and U have the same transverse behaviour $\Phi(y)$; this is a direct consequence of (12.1); ζ_0 and U_0 are constant amplitudes. Since V vanishes throughout, the side boundary conditions are automatically satisfied. Substituting (12.2) into (12.1) yields

$$\left.\begin{aligned} c_{\mathrm{ph}} &= \frac{\omega}{k} = \pm\sqrt{g h_{\mathrm{bar}}}, \\ \zeta_0 &= \sqrt{\frac{h_{\mathrm{bar}}}{g}}\, u_0, \\ \frac{\mathrm{d}\Phi}{\mathrm{d}y} + \frac{f}{c_{\mathrm{ph}}}\Phi = 0 \quad &\Rightarrow \quad \Phi = \exp\left(-fy/c_{\mathrm{ph}}\right). \end{aligned}\right\} \tag{12.3}$$

The first is the shallow water dispersion relation whose frequencies may be sub- or super-inertial, the second relates the amplitude of the free surface displacement with that of the x-velocity component, and the third yields the transverse variation of ζ and U. It follows that the amplitudes of ζ and U decay exponentially as one moves away from the side boundary. The decay rate is given by the *Rossby radius of deformation* or in brief the *Rossby radius*

$$R = \frac{c_{\mathrm{ph}}}{f} = \frac{\sqrt{g h_{\mathrm{bar}}}}{f} = \frac{\sqrt{g h_{\mathrm{bar}}}}{2\Omega \sin\phi}. \tag{12.4}$$

Its value depends on the Coriolis parameter and the size of the phase speed c_{ph}, which in turn itself depends on $h_{\mathrm{bar}} = H$ (for barotropic waves). Typical values are given in Table 12.1. R grows according to a square root law with the water depth, and it decays with $\sin^{-1}\phi$, where ϕ is the geographical latitude. These waves are called *Kelvin waves* in honor of Lord Kelvin,[2] who in 1879 [12] in a paper entitled

Table 12.1 Typical values of the Rossby *radius of deformation* (in km) for *barotropic* motions depending on water depth and geographical latitude to the North or South, values in (km)

$\Phi(^\circ)$ \ H(m)	20	50	100	200	500	1,000	2,000
10	553	874	1,236	1,749	2,765	3,910	5,530
20	280	444	627	888	1,404	1,985	2,808
30	192	303	429	607	960	1,358	1,920
40	149	236	334	472	747	1,056	1,494
50	125	198	280	396	626	886	1,253
60	110	175	247	350	554	784	1,109
70	102	161	228	323	511	722	1,022
80	97	154	218	308	487	689	975

[2] For a biographical sketch see Fig. 12.1.

'On gravitational oscillations of rotating water' provided the basis for all rotation affected waves on the f-plane.

We have mentioned above that the regions of applicability of the above solution can also be channels with constant water depth and constant width B. This is now clear from the solution (12.2), (12.3), since $V \equiv 0$ identically vanishes. At any position $y = B$ a vertical wall may be inserted that is parallel to the x-axis without violating the solution. The exponential decay of ζ and U in the transverse direction with an e-folding width of the size of the Rossby radius of deformation thus requires a channel to have a width of the size of this Rossby radius of deformation or larger in order that such a decay may become observable by measurement. The Great Lakes in US/Canada, the Caspian Sea and the Baltic Sea are of this size but Lake Ladoga and Lake Onega – the two largest lakes in Europe – are perhaps a bit too small.

Figure 12.2 depicts the behaviour of the solution (12.2) and (12.3). These waves are non-dispersive and propagate with the same phase speed as do shallow water waves without rotation. They are *coastal trapped* and have boundary layer structure if the basin width is sufficiently large relative to the Rossby radius of deformation. At small channel widths relative to the Rossby radius of deformation we have $\Phi(y) \approx 1$, and the Kelvin wave becomes an ordinary long gravity wave. Furthermore, since there are only x- and z-components of the velocity vector, the fluid particle trajectories traverse elliptical orbits in vertical planes. Finally, if the wave propagates in the negative x-direction ($\omega < 0$), then the phase speed is $c_{\mathrm{ph}} = -\sqrt{gh_{\mathrm{bar}}}$, and so, the attenuation is in the negative y-direction. Both situations can be described as follows: The Kelvin *wave amplitudes of ζ and U are transversely attenuated to the right (left) on the Northern (Southern) hemisphere when looking into the direction of propagation of the wave.*

Problem 12.1 *Consider (12.1) with $V \equiv 0$. From $(12.1)_{1,2}$, which we write now as*

$$\frac{\partial \zeta}{\partial t} + \frac{\partial U}{\partial x} = 0, \quad \frac{\partial U}{\partial t} = -gh_{\mathrm{bar}} \frac{\partial \zeta}{\partial x} \tag{12.5}$$

the zeroth order approximation ζ_0, U_0

$$\begin{aligned} U_0 &= A_0 \exp\left[i(kx - \omega t)\right], \\ \zeta_0 &= B_0 \exp\left[i(kx - \omega t)\right] \end{aligned} \tag{12.6}$$

in which

$$B_0 = \frac{k}{\omega} A_0, \qquad \frac{\omega^2}{k^2} = c_{\mathrm{ph}}^2 = gh_{\mathrm{bar}} \tag{12.7}$$

can be derived. Here, A_0 and B_0 do not show any y-dependence. Equation $(12.1)_3$ allows to use the above solution for U_0 to derive the equation

$$\frac{\partial \zeta_1}{\partial y} = -\frac{f}{gh_{\mathrm{bar}}} U_0 \tag{12.8}$$

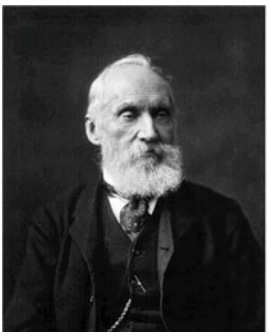

Fig. 12.1 William Thomson, first Baron Kelvin (1824–1907). A Kelvin–Helmholtz instability rendered visible by clouds over Mount Duval in Australia. Photos from http://en.wikipedia.org/.

William Thomson, first Baron Kelvin or Lord Kelvin, or Kelvin of Largs (26 June 1824, Belfast, Northern Ireland, 17 December 1907, Netherhall at Largs) was a mathematical physicist and engineer. He was professor of Natural Philosophy at Glasgow University for more than 50 years and did important work in the mathematical analysis of electricity and the formulation of the first and second law of thermodynamics. He also had a successful career as an electrical telegraph engineer which propelled him into the public eye and ensured his wealth, fame and honour. Largely for this work he was knighted by Queen Victoria (1866), becoming Sir Willliam. Moreover, for his scientific key role in developing the basis of the absolute temperature and the Kelvin temperature scale, and because of his opposition to the Irish Home Rule, he received ennoblement as Baron Kelvin of Largs or Lord Kelvin (1892).

As a child William Thomson lost his mother at the age of 6 years (1830). The four boys and two girls who survived infancy were educated by their father who was a mathematics and engineering teacher at the Royal Belfast Academic Institution. In 1834, the father became professor at Glasgow University. So, son William started his university education in Glasgow at the age of 10. In the academic year 1839–1840, he won the class prize in Astronomy for his essay on the figure of the Earth, which showed an early talent for mathematical analysis and creativity. When coming across Fourier's *Théorie analytique de la chaleur* he committed himself to study continental mathematics. Between 1841 and 1842 he wrote under the pseudonym P.Q.R. three papers on the theory of heat and its connection with electricity. He left Glasgow University in 1841 without a degree and went with his father's strong support to Cambridge, where he graduated in 1845 in second place and also won the Smith's Prize. In the same year, he also became a fellow of Peterhouse but left Cambridge in 1846, when, at the age of 22, he was appointed to the chair of Natural Philosophy in the University of Glasgow, a position he kept until 1899.

William Thomson's important work on the first and second law of thermodynamics was done in the years from 1847 onwards during about 10 years. Besides his fundamental work on absolute zero, he and James Prescott Joule collaborated, one result being the Joule–Thomson effect. He also phrased the second law in the form: *It is impossible, by means of inanimate material agency, to derive mechanical effect from any portion of matter by cooling it below the temperature of the coldest of the surrounding objects*.

Thomson did also major work on electricity and developed his Thomson bridge, Kelvin generator, mirror galvanometer and many more. He was deeply involved in the proper build-up of the telegraph cable across the Atlantic, involving serious professional disputes with Wildman Whitehouse, the electrician of the Atlantic Telegraph Company and his eventual triumph and Whitehouse's disaster and dismissal. Thomson was also an enthusiastic yachtsman and contributed to the perfection to many marine instruments. His interest in tides led to the description of Kelvin waves and the Thomson tide predicting machine.

Thomson published more than 600 scientific papers and filed 70 patents. His book 'Treatise on Natural Philosophy' (1867) with Peter Guthrie Tait did much in unifying the modern physics of that time.

The text is based on:

http://de.wikipedia.org/wiki/Lord_Kelvin

http://en.wikipedia.org/wiki/Lord_Kelvin.

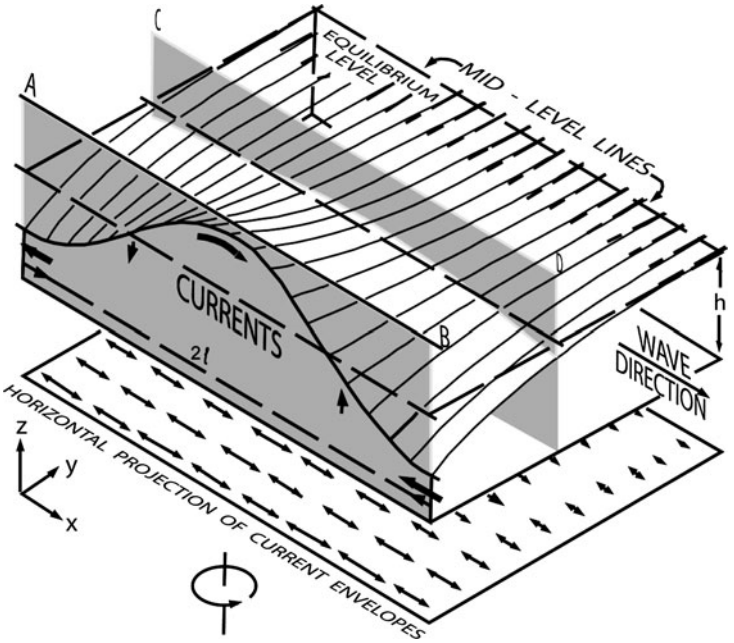

Fig. 12.2 Long Kelvin wave in a semi-infinite half space x, y, propagating in the positive x-direction in an uniform depth model. The vertical plane AB defines the shore of a layer of infinite width. The vertical plane CD parallel to AB may also form a shore line adapted from [27], with changes. © Center for Great Lake Studies (now Great Lakes WATER Institute), reproduced with permission

from which

$$\zeta_1 = -\frac{f}{gh_{\text{bar}}} U_0 y \tag{12.9}$$

is obtained. This demonstrates that for longitudinal motions the free surface must be transversely inclined in order that the transverse pressure gradient can balance the Coriolis force. Show that by continuing this iteration procedure, the following expressions are obtained:

$$\begin{aligned} U &= A_0 \left\{ 1 - \left(\frac{y}{R}\right) + \frac{1}{2!}\left(\frac{y}{R}\right)^2 - \frac{1}{3!}\left(\frac{y}{R}\right)^3 \pm \cdots \right\} \exp\left[i\left(kx - \omega t\right)\right] \\ &= A_0 \exp\left(-\frac{y}{R}\right) \exp\left[i\left(kx - \omega t\right)\right], \\ \zeta_0 &= B_0 \left\{ 1 - \left(\frac{y}{R}\right) + \frac{1}{2!}\left(\frac{y}{R}\right)^2 - \frac{1}{3!}\left(\frac{y}{R}\right)^3 \pm \cdots \right\} \exp\left[i\left(kx - \omega t\right)\right] \\ &= B_0 \exp\left(-\frac{y}{R}\right) \exp\left[i\left(kx - \omega t\right)\right], \end{aligned} \tag{12.10}$$

which is the same as (12.2) and (12.3). Here $R = c_{\text{ph}}/f$. ◆

This iterative construction has been pursued in practice only to first order in y. It is called *Kelvin wave dynamics*, has been introduced by Defant [9] and applied by him in the seiche analysis of Lake Michigan and later by Platzman and Rao [28] in an analysis of surface seiches of Lake Erie.

The method of Kelvin wave dynamics has found its ultimate application in the construction of extended channel models of Raggio and Hutter [35–37], and Hutter and Raggio [38], a kind of Chrystal-equations for elongated lakes on the rotating Earth. In these models the governing equations (12.1) are written in curvilinear coordinates, in which one axis follows the long direction of the lake (approximately the thalweg), whilst the other axis is perpendicular and transverse to this long axis. Raggio and Hutter perfected this method by a formal procedure using the method of weighted residuals, which allows determination of as many transverse elements of the analogue representations to (12.10) as desired. A full account on this class of channel modes is given in Chap. 22.

12.2.1 Pseudo-Standing Kelvin Waves

In a non-rotating fluid layer of constant depth, standing waves do exist. In fact such standing waves were constructed in Sects. 7.2 and 7.3, see Figs. 7.9, 7.12 of Volume I. Their distinctive feature is that spatially fixed nodal lines x=const. do exist, across which no water will move at any one time. In an infinite channel of constant width, exact standing Kelvin waves (in a rotating channel) *do not exist*. What exists is something 'close to standing waves': they will subsequently be called *pseudo-standing Kelvin waves*.[3] To construct their solution, consider a forward propagating Kelvin wave with large amplitudes at $y = 0$ and decaying as y grows, and a backward moving Kelvin wave with large amplitudes at $y = B$ and decaying as $(B - y)$ decreases. These waves are given by

$$(\zeta, u)_{\text{forward}} = \left(\frac{c_{\text{ph}}}{g}u_0, u_0\right) \exp\left(-\frac{fy}{c_{\text{ph}}}\right) \exp\left[i\left(kx - \omega t\right)\right],$$
$$(\zeta, u)_{\text{backward}} = \left(\frac{c_{\text{ph}}}{g}u_0, -u_0\right) \exp\left(-\frac{f(B-y)}{c_{\text{ph}}}\right) \exp\left[i\left(kx + \omega t\right)\right]. \tag{12.11}$$

Adding the two waves and taking real parts yields

[3] In the literature such pseudo-standing waves are for brevity often simply called standing waves; we believe this convention is more confusing than convenient.

$$\begin{aligned}\zeta &= \Re e\{\zeta_{\text{forward}} + \zeta_{\text{backward}}\} \\ &= \frac{2c_{\text{ph}}}{g} u_0 \exp\left(-\frac{fB}{2c_{\text{ph}}}\right)\left\{\cosh\left[\frac{f}{c_{\text{ph}}}\left(\frac{B}{2}-y\right)\right]\cos kx\cos\omega t\right. \\ &\qquad \left. + \sinh\left[\frac{f}{c_{\text{ph}}}\left(\frac{B}{2}-y\right)\right]\sin kx\sin\omega t\right\}, \\ u &= \Re e\{u_{\text{forward}} + u_{\text{backward}}\} \\ &= 2u_0 \exp\left(-\frac{fB}{2c_{\text{ph}}}\right)\left\{\sinh\left[\frac{f}{c_{\text{ph}}}\left(\frac{B}{2}-y\right)\right]\cos kx\cos\omega t\right. \\ &\qquad \left. + \cosh\left[\frac{f}{c_{\text{ph}}}\left(\frac{B}{2}-y\right)\right]\sin kx\sin\omega t\right\}.\end{aligned} \tag{12.12}$$

The solution (12.12) enjoys the following properties (compare Figs. 12.3 and 12.4).

- For $y = B/2$ and $x = (2n+1)\pi/(2k)$, $\zeta = 0$ for all time. Any of these points, called *amphidromic points* or *amphidromes*, is characterized by the fact that the surface never experiences any elevation from its equilibrium level.
- For $y = B/2$ and $x = n\pi/k$ (these are the points on the centre line between two amphidromic points) the velocity vanishes at all times.
- At times $t = n\pi/\omega$ the surface elevation ζ (velocity u) is symmetrically (anti-symmetrically) distributed across the channel width with maximum velocities arising at the shore lines at positions x midway between the amphidromic points. Similarly, for $t = ((2n+1)\pi/(2\omega))$, ζ is anti-symmetrically distributed, whilst u is symmetrically distributed across the channel.
- Lines of *constant elevation amplitudes* – the so-called *co-range lines* – are given by

$$\cosh^2\left[\frac{f}{c}\left(\frac{B}{2}-y\right)\right]\cos^2(kx) + \sinh^2\left[\frac{f}{c}\left(\frac{B}{2}-y\right)\right]\sin^2(kx) = \text{const.} \tag{12.13}$$

  These lines are dashed in Fig. 12.4. In the vicinity of the amphidrome they encircle the amphidromic point, farther away they are oscillatory.
- Lines of *constant phase* – the so-called *co-tidal lines* – are described instead by

$$\tan\phi = \tan(kx)\tanh\left[\frac{f}{c}\left(\frac{B}{2}-y\right)\right] = \text{const.} \tag{12.14}$$

  It is easily seen that these are lines through the amphidromic points. Co-tidal lines which differ in phase from one another by the angle π are centro- symmetrically arranged with respect to the amphidromic point.

All these properties can with little effort be deduced from the respective formulae, and they are easily corroborated in Figs. 12.3 and 12.4. The former

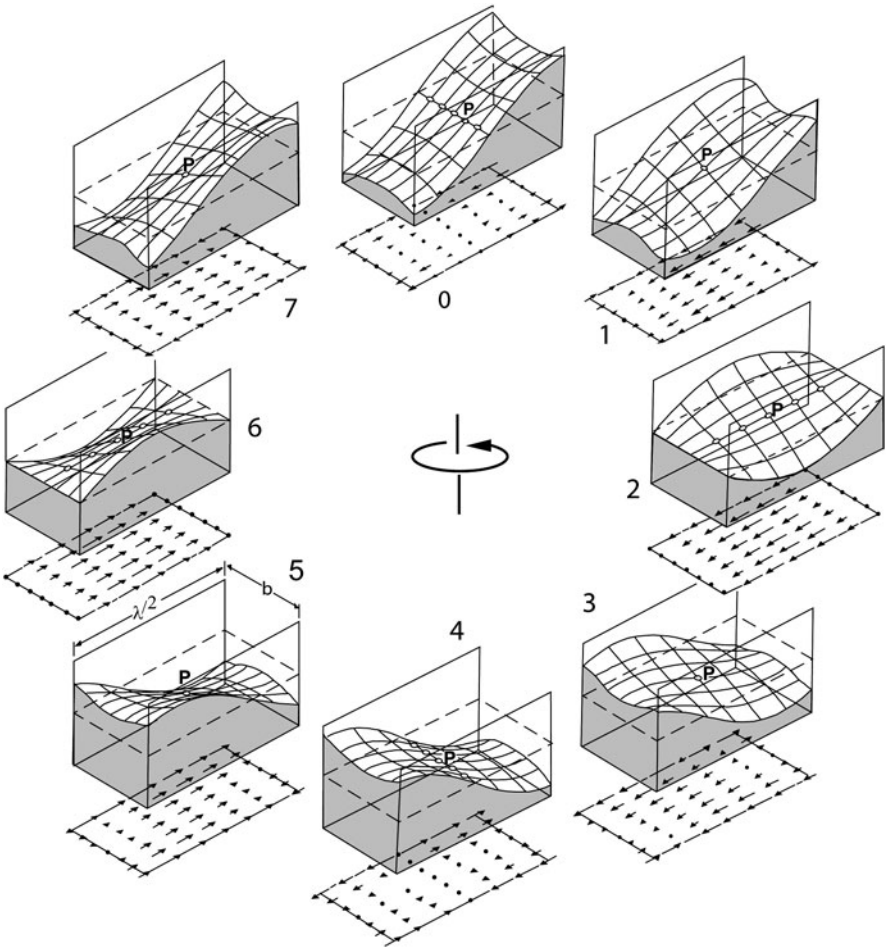

Fig. 12.3 Successive phases (1/8 cycle) of a long, standing, amphidromic wave in a straight rotating channel of rectangular cross section. Horizontal components of the wave current are projected on the plane below the channel. The amphidromic point P of zero elevation change, around which the wave rotates counter-clockwise, is in the centre (redrawn from Mortimer, 1974 [24]. © Int. Ver. Theor. Angew. Limnol., http://www.schweizerbart.de)

of these displays the distribution of the surface elevation and longitudinal velocity in successive phases of (1/8)-cycle of such an amphidromic wave. The figure illustrates the cyclonic (anticlockwise on the Northern Hemisphere) propagation of the wave: In one period of its motion, the wave crest moves around the amphidromic point and the velocity moves forth and back along the channel. The velocities are weakest along lines transverse to the channel and midway between the amphidromic points; however *there is no line across the channel at which the longitudinal velocity would vanish for all time*. It follows that gravity waves in a gulf or a closed basin cannot simply be obtained by superimposing Kelvin waves. We shall soon return to this point.

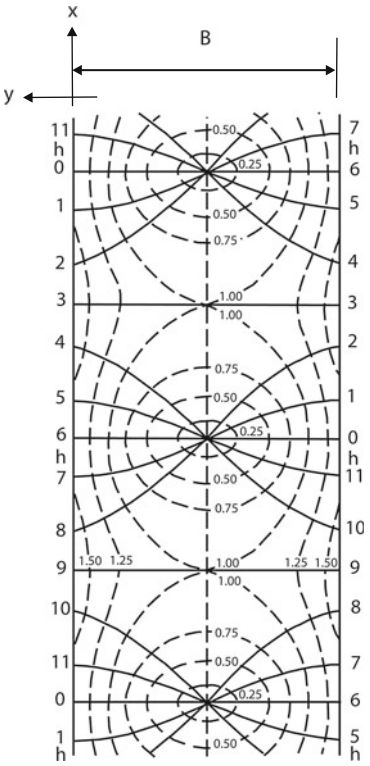

Fig. 12.4 Amphidromic system in an infinitely long canal, resulting from superposition of two Kelvin waves of 12-h period, traveling in opposite directions. *Full lines*: co-tidal lines in hours: *broken lines*: co-range lines (Z_0=0.5, $k = 1$, $f/c = 0.7$, corresponding to a canal width of 400 km, $H = 40$ m). © Courtesy W. Krauss (1966) [14], http://www.schweizerbart.de

12.2.2 Baroclinic Kelvin Waves

So far in this chapter only barotropic Kelvin waves were studied. In Chap. 11 it was, however, shown that in a *strictly vertically stratified fluid layer of constant depth in the shallow water approximation* the horizontal and the vertical problem can be separated such that the vertical eigenvalue problem, formulated, say, for the vertical velocity component, determines the equivalent depths h_n, where n is a counting index which identifies the baroclinic mode number. This equivalent depth then enters the horizontal problem which determines the propagation properties in the horizontal direction.

For instance, in the *two layer variable depth model*, the baroclinic analogue of the linearized governing equations are given by (11.98). The equations are exactly the same equations as (12.1) with gh_{bar} replaced by gh_{int}, where

$$h_\alpha = \begin{cases} h_{\text{ext}} = H, & \text{barotropic case,} \\ h_{\text{int}} = \varepsilon \dfrac{H_1 H_2}{H_1 + H_2}, & \text{2-layer, baroclinic case} \end{cases} \tag{12.15}$$

Table 12.2 Equivalent depth factors r and $\sqrt{r}$ for the first baroclinic mode for a selected number of ratios H_2/H_1

H_2/H_1	r	$\sqrt{r}$	H_2/H_1	r	$\sqrt{r}$
0.1	0.0909	0.3015	5.0	0.8333	0.9129
0.5	0.3333	0.5774	10.0	0.9091	0.9535
1.0	0.5000	0.7071	100.0	0.9901	0.9950
			∞	1.000	1.000

is the equivalent depth of the two layer model in the barotropic and baroclinic modes, respectively and $\varepsilon = \Delta\rho/\rho$. So, the Kelvin wave solutions are equally analogous and given by

$$\begin{aligned} \zeta_\alpha &= \sqrt{\frac{h_\alpha}{g}} u_0 \exp\left(-\frac{f}{\sqrt{gh_\alpha}} y\right) \exp\left[i\left(kx - \omega t\right)\right], \\ U_\alpha &= u_0 h_\alpha \exp\left(-\frac{f}{\sqrt{gh_\alpha}} y\right) \exp\left[i\left(kx - \omega t\right)\right] \end{aligned} \tag{12.16}$$

with the corresponding Rossby radius of deformation

$$R_{\text{eq}} = \begin{cases} R_{\text{ext}} = \sqrt{gH}/f, & \text{barotropic case,} \\ R_{\text{int}} = \sqrt{gh_{\text{int}}}/f, & \text{baroclinic case.} \end{cases} \tag{12.17}$$

Writing

$$h_{\text{int}} = \frac{1}{1 + H_1/H_2} H_1\varepsilon = rH_1\varepsilon, \quad r = \frac{H_2/H_1}{H_2/H_1 + 1}, \quad \varepsilon = \frac{\rho_2 - \rho_1}{\rho_*}, \tag{12.18}$$

the equivalent depth, h_{int} is written as a quantity proportional to $H_1\varepsilon$. Table 12.2 lists a few values of r and $r^{1/2}$; $H_1\varepsilon$ is the equivalent depth, h_{int} in the limit as $H_2/H_1 \to \infty$.

So, for rough estimates we may set

$$\begin{aligned} h_{\text{int}} &= rH_1\varepsilon, \\ c_{\text{ph}}^{\text{int}} &= \sqrt{rgH_1\varepsilon} = \sqrt{r}\sqrt{gH_1\varepsilon} = \sqrt{r}(c_{\text{ph}}^{\text{int}})_{\max}, \\ R_{\text{int}} &= \frac{\sqrt{rgH_1\varepsilon}}{f} = \sqrt{r}\frac{\sqrt{gH_1\varepsilon}}{f} = \sqrt{r}R_{\text{int}}^{\max}, \end{aligned} \tag{12.19}$$

in which $R_{\text{int}}^{\max}$ is the internal Rossby radius of deformation. Values of $(c_{\text{ph}}^{\text{int}})_{\max}$ lie in the interval between approximately $10^{-2}\,\text{ms}^{-1}$ and $10\,\text{ms}^{-1}$. Figure 12.5 displays $R_{\text{int}}^{\max}$ as a function of the maximum phase speed $(c_{\text{ph}}^{\text{int}})_{\max} = \sqrt{gH_1\varepsilon}$ for various

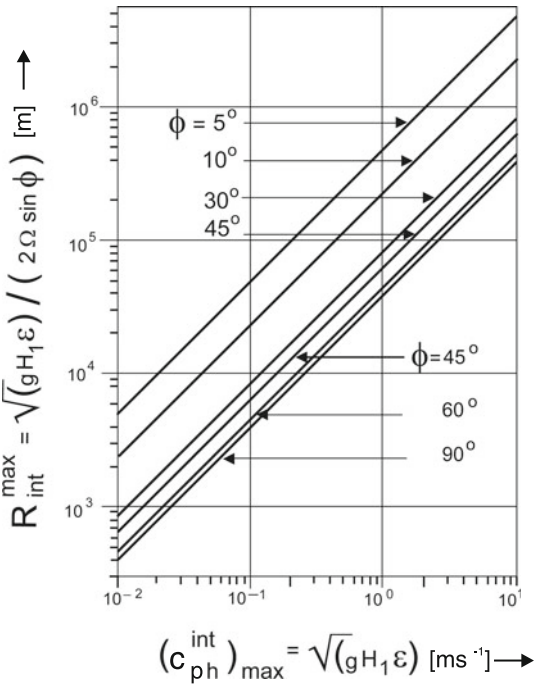

Fig. 12.5 Maximum internal Rossby radius of deformation as a function of the maximum internal phase speed $\sqrt{gH_1\varepsilon}$ for various latitude angles

values of the geographical latitude. For a specific two-layer stratification with depth ratio H_2/H_1, the adequate phase speeds and Rossby radii of deformation are then obtained by multiplication with $\sqrt{r}$.

12.3 Inertial Waves

Kelvin waves are long shallow water waves on the rotating Earth whose horizontal projection of the particle motion is purely longitudinal. Because of the Coriolis forces such an unidirectional motion can only be maintained when the surface elevation experiences an inclination in the direction perpendicular to the wave propagation. This transverse variation of the surface elevation, due to geostrophic adjustment, is exponentially evanescent as one moves away from the boundary. In an infinite basin, there are no boundaries that can sustain a deviation of ζ from its position at rest. Plane waves in infinite three-dimensional space (with constant wave amplitude perpendicular to the direction of wave propagation) were treated in Chap. 11, Sect. 11.4. A special case of these waves are the *inertial waves*. Their properties can be deduced from (12.1) by imposing the condition that their surface elevation vanishes, $\zeta \equiv 0$; so, all motion is purely horizontal. With $\zeta = 0$, (12.1) take the forms

$$\left.\begin{aligned} \frac{\partial U}{\partial x} + \frac{\partial V}{\partial y} &= 0, \\ \frac{\partial U}{\partial t} - fV &= 0, \\ \frac{\partial V}{\partial t} + fU &= 0, \end{aligned}\right\} (x, y, t) \in \mathbb{R}^2 \cup \mathbb{R}^+. \tag{12.20}$$

With the harmonic representation

$$(U, V) = (U_0, V_0)\exp\left[i(\boldsymbol{k} \cdot \boldsymbol{x} - \omega t)\right] \tag{12.21}$$

it is then readily shown that

$$\begin{aligned} &kx + ly = 0, \qquad \text{where} \quad \boldsymbol{k} = (k, l), \\ &-i\omega U_0 - fV_0 = 0, \; -i\omega V_0 + fU_0 = 0, \end{aligned} \tag{12.22}$$

from which one concludes that $\omega = f$, (independent of $\boldsymbol{k}$); hence, the wavenumber is arbitrary ($\boldsymbol{k}$ is perpendicular to the horizontal position vector (x, y)). This also implies that the phase speed $c = \omega/|\boldsymbol{k}|$ is arbitrary. Moreover,

$$\begin{aligned} U &= \Re e\{U_0 \exp\left[i(\boldsymbol{k} \cdot \boldsymbol{x} - \omega t)\right]\}, \\ V &= \Re e\{-iU_0 \exp\left[i(\boldsymbol{k} \cdot \boldsymbol{x} - \omega t)\right]\}, \\ \text{or} \qquad & \\ U &= \Im m\{U_0 \exp\left[i(\boldsymbol{k} \cdot \boldsymbol{x} - \omega t)\right]\}, \\ V &= \Im m\{-iU_0 \exp\left[i(\boldsymbol{k} \cdot \boldsymbol{x} - \omega t)\right]\}. \end{aligned} \tag{12.23}$$

This shows that particle motions are horizontal and circular with clockwise propagation in the Northern hemisphere, and the trajectory radius is $R = c/f$. These results may be summarized as follows:

Properties of Inertial Waves

- *The angular frequency equals the inertial frequency: $\omega = f$. This fact explains why these waves are called inertial waves.*
- *The wave speed is not restricted, i.e. these waves may have arbitrary wavenumber.*
- *Particle trajectories are horizontal circles with diameter $R = c_{\text{ph}}/f$ where c_{ph} is the phase speed; this radius is akin to the Rossby radius of deformation, its difference to the latter being that here c_{ph} is not explicitly specified, but may have any value.*

12.4 Poincaré Waves

Kelvin waves have the property that water particle displacements are strictly longitudinal, whilst inertial waves are circular. There are many other solutions of (12.1) which, when conveniently combined, fit particular boundary conditions [27, 29]. These solutions are described by the harmonic representation

$$(\zeta, U, V) = (\zeta_0, U_0, V_0)\exp\left[i\left(\boldsymbol{k}\cdot\boldsymbol{x} - \omega t\right)\right] \tag{12.24}$$

with the horizontal wavenumber vector $\boldsymbol{k}\hat{=}(k,l)$. Substituting (12.24) into (12.1) leads to a homogeneous linear system of equations for (ζ_0, U_0, V_0) which possesses the solution

$$\begin{aligned} U_0 &= -\frac{gh_n}{\omega^2 - f^2}(-k\omega + ifl)\zeta_0, \\ V_0 &= -\frac{gh_n}{\omega^2 - f^2}(-ikf - l\omega)\zeta_0, \end{aligned} \tag{12.25}$$

for arbitrary ζ_0, provided its determinant vanishes, which is the case, if

$$\omega^2 = f^2 + gh_n(k^2 + l^2). \tag{12.26}$$

'The general solution (12.25) and (12.26) is formally valid when k and l are complex valued; k and l can be real or imaginary, subject to the condition for pure harmonic waves that ω and $(k^2 + l^2)$ must be real. If, for a wave travelling in the x-direction k is real and positive and l is purely imaginary [to make this explicit, we may replace l by il'] a special class of progressive wave solutions appears [...], characterized by a sinusoidal variation of the wave amplitude in the x-direction and an exponential variation in the y-direction. But, if both k and l are real, and for convenience the direction of propagation is made to coincide with the x-axis, so that $k = k_h$ and $l = 0$ in a plane wave) the Sverdrup wave emerges with sinusoidal amplitude variation along x and no amplitude variation along y $(l = 0)$', after Mortimer [27]. All these solutions are summarized in Fig. 12.6 and the following problem.

Problem 12.2 *Show that the dispersion relation (12.26) can, alternatively, be written as*

$$y = (x^2 + 1 - a^2)^{1/2}, \tag{12.27}$$

$$y := \left|\frac{\omega}{f}\right|, \quad x := \frac{\sqrt{gh_n}k}{f}, \quad a^2 := \frac{gh_n l'^2}{f^2}. \tag{12.28}$$

Show, moreover, that for different values of the transverse wavenumber parameter a^2, the graphs of (12.27) are as shown in Fig. 12.6.

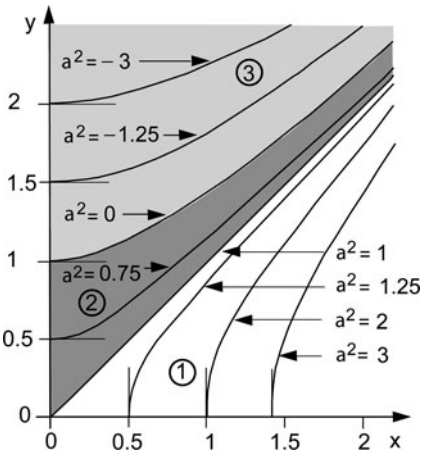

Fig. 12.6 Frequency, $y = |\omega/f|$ vs. wavenumber, $x = \sqrt{gh_n}k/f$, diagram. Regions (1)+(2) are the regime of transversely exponentially growing or evanescing waves, regime (3) is the regime of oscillatory waves, see also main text

- *Regime (1),* $1 < a^2$*: Graphs of (12.27) are branches of hyperbolas with vertices on the x-axis and asymptote* $y = x$ *(white triangle bounded by* $y = 0$ *and* $y = x$ *in Fig. 12.6.*
- *Regime (2),* $0 < a^2 < 1$*: Graphs of (12.27) are branches by hyperbolas with vertices on the y-axis and asymptote* $y = x$ *(dark-shaded region bounded by* $y = x$ *and the hyperbola for* $a^2 = 0$*. Note that in regimes (1) and (2) the transverse wavenumbers* l' *are real and corresponding waves transversely exponentially growing or evanescing.*
- *Regime (3),* $a^2 < 0$*: Graphs of (12.27) are branches of hyperbolas as shown in the light gray region of Fig. 12.6. In this region, wave crests are transversely harmonically varying* $(a^2 < 0)$*, but constant for* $a^2 = 0$*.* ◆

Platzman [29] and Mortimer [27] call waves in regime (3) Sverdrup waves; they have $l'^2 < 0$ (or $l^2 > 0$) and are, therefore, transversely oscillatory. It is obvious that by rotation of the coordinate system from (x, y) to $(\bar{x}, \bar{y})$ the direction of increasing $\bar{x}$ can be made to agree with the direction of wave progress, in which case $\bar{k} > 0$ and $\bar{l} = 0$. The corresponding solution for the surface elevation ζ and horizontal transports U, V can be obtained from (12.24) to (12.26). (We use overbars to indicate that the rotated coordinates $(\bar{x}, \bar{y})$ are used, for which $\bar{l} = 0$). Results are collected in Problem 12.3.

Problem 12.3 *Write (12.24)–(12.26) in a Cartesian coordinate system* $(\bar{x}, \bar{y})$ *for which wave progression is in the* $\bar{x}$*-direction* ($\bar{l} = 0$)*, and prove that*

$$
\begin{aligned}
&(\bar{\zeta}, \bar{U}, \bar{V}) = (\bar{\zeta}_0, \bar{U}_0, \bar{V}_0)\exp[i(kx - \omega t)],\\
&\bar{U}_0 = \frac{\omega}{k}\bar{\zeta}_0, \quad V_0 = -i\frac{f}{k}\bar{\zeta}_0,\\
&\omega^2 = f^2 + gh_n k^2.
\end{aligned}
\tag{12.29}
$$

Taking real or imaginary values, (12.29) take the forms

$$\begin{aligned}\bar{\zeta} &= \bar{\zeta}_0[\cos(kx-\omega t),\ \sin(kx-\omega t)],\\ \bar{U} &= \frac{\omega}{k}\bar{\zeta}_0[\cos(kx-\omega t),\ \sin(kx-\omega t)],\\ \bar{V} &= \frac{f}{k}\bar{\zeta}_0[\sin(kx-\omega t),\ -\cos(kx-\omega t)],\end{aligned} \tag{12.30}$$

where the brackets $[\alpha\,,\beta]$ *are obtained from the real and imaginary parts, respectively. Using* $\bar{U} = H\bar{u}$, $\bar{V} = H\bar{v}$, *where* H *is the water depth, and the continuity equation*

$$\frac{\partial \bar{U}}{\partial x} + \frac{\partial}{\partial z}(H\bar{w}) = 0 \tag{12.31}$$

show, moreover, that for $n = 1$

$$\bar{w} = -\frac{\omega}{H}(z+H)\bar{\zeta}_0[\sin(kx-\omega t),\ -\cos(kx-\omega t)], \tag{12.32}$$

satisfying the boundary conditions $\bar{w}(z=-H) = 0$ *and* $\bar{w}(z=0) = \partial\zeta/\partial t$. *The linear variation of* $\bar{w}$ *with* z *over the depth is a consequence of the shallow water approximation.* ◆

Beyond this problem solution it can also be shown that particle trajectories are as shown for the more general stratified case in Fig. 11.9. Here, we mention once more that the Sverdrup wave, comprising regime (3) of Fig. 12.6 is a member of a more general class, treated by Poincaré [31],[4] and has been referred to as a Poincaré wave, e.g. by LeBlond and Mysak [18] as are all super-inertial waves covered in Fig. 12.6. Mortimer [27] writes 'However, others [22, 23, 29] find it convenient to confine the designation 'Poincaré' to waves which satisfy the boundary conditions at a straight vertical wall or walls in rotating uniform-depth models', and he demonstrates in a careful analysis that Poincaré waves so defined can be constructed as combinations of Sverdrup waves.

This is exactly, what we are now going to do. More specifically, we construct wave solutions of (12.1) which satisfy the boundary conditions $V = 0$ at the channel walls, but may have non-trivial transverse velocity component inside the channel. To this end, we eliminate U and ζ from (12.1) and seek plane wave solutions for

$$V = V_0(y)\exp[i(kx-\omega t)]. \tag{12.33}$$

The reader may verify that elimination of U and ζ from (12.1) yields

$$\left(\frac{\partial V}{\partial x^2} + \frac{\partial^2 V}{\partial y^2}\right) - \frac{1}{gh_n}\left(\frac{\partial^2}{\partial t^2} + f^2\right)V = 0 \tag{12.34}$$

[4] For a biographical sketch see Fig. 12.7.


COURS DE LA FACULTÉ DES SCIENCES DE PARIS.

LEÇONS

DE

MÉCANIQUE CÉLESTE

PROFESSÉES A LA SORBONNE

PAR

H. POINCARÉ,

TOME I.

THÉORIE GÉNÉRALE DES PERTURBATIONS PLANÉTAIRES.

PARIS,

GAUTHIER-VILLARS, IMPRIMEUR-LIBRAIRE

1905

Fig. 12.7 Jules Henri Poincaré (1854–1912), photographic portrait by Henri Manuel (from http://en.wikipedia.org/), and the front page of his 'Lectures on Celestial Mechanics' (image from Cornell University Library http://dlxs2.library.cornell.edu/).

Jules Henri Poincaré (29 April 1854, Meurthe-et-Moselle, near Nancy; 17 July 1912, Paris) was a French mathematician, theoretical physicist, mining engineer and philosopher of Science. During his childhood, he was seriously ill for a time with diphtheria. He received his first education from his mother. From 1862 to 1873 he attended the Lycée in Nancy, where his outstanding talents in all fields except music and physical education were noted, in particular the superiority in mathematics. Henri Poincaré spent the Franco-Prussian war of 1870 with his father in the Ambulance Corps. In 1873, he entered École Polytechnique, where he became a student of Charles Hermite. He graduated in 1875 (or 1876), but went on to study at the École des Mines, continuing with his mathematical studies in addition to the mining engineering syllabus, receiving the engineering degree in 1879. At the same time Poincaré was preparing for his doctorate in mathematics under Hermite. His thesis is in the field of differential equations, and the University of Paris (Sorbonne) granted him the Ph.D. in 1879. In 1881, he married Miss Poulain d'Andecy, and they had four children.

Poincaré started his professional career as a mathematics lecturer at Caen University, while simultaneously also working at the Ministry of Public Service from 1881 to 1885. He climbed up the latter as a mining engineer to chief engineer in 1893 and inspector general in 1910. Beginning in 1881 and for the remainder of his career he taught at the Sorbonne, where he eventually held the chairs of Physical and Experimental Mechanics, Mathematical Physics, Theory of Probability and Celestial Mechanics and Astronomy.

In 1887, Poincaré was elected to the French Academy of Sciences. He became its president in 1906, and was elected to the Académie Française. In 1887, he also won Oscar II, King of Sweden's mathematical competition for a resolution of the three-body problem concerning the free motion of multiple orbiting bodies, and in 1893 he joined the French Bureau des Longitudes, which engaged him in the synchronization of the time around the world. On 17 July 1912, Poincaré died of an embolism after prostate surgery.

Henri Poincaré is considered 'The Last Universalist', since he excelled in all fields of the discipline as it existed in his time. He worked not only on many subjects of pure mathematics but also other subjects of mathematical physics. He was the first to present the Lorentz transformation of the theory of special relativity (1896). A nice detailed reference to his work is given in the URL address below. The fluid waves named after him are briefly mentioned in a footnote of his book 'Celestial Mechanics'; they form now an important class of waves in meteorology, oceanography and limnology.

The text is based on: http://en.wikipedia.org/wiki/Jules_Henri_Poincare

and substitution of (12.33) in (12.34) leads to the eigenvalue problem

$$\begin{aligned} &V_0'' + \left(\frac{\omega^2 - f^2}{gh_n} - k^2\right) V_0 = 0, \quad 0 \leqslant y < B, \\ &V_0 = 0, \quad \text{at} \quad y = 0 \quad \text{and} \quad y = B. \end{aligned} \tag{12.35}$$

for the distribution of V across the channel. In the above, the prime denotes differentiation with respect to y, and B is the channel width. Depending on the value of h_n ($=H$ for the barotropic mode, $=h_n$ for the baroclinic mode) (12.33), (12.35) describe the barotropic and baroclinic progressing Poincaré waves. The solution of (12.35) is

$$V_0 = \bar{V} \sin\left(\frac{m\pi y}{B}\right), \qquad (m = 1, 2, 3, \ldots) \tag{12.36}$$

with the dispersion relation

$$k^2 = \frac{\omega^2 - f^2}{gh_n} - \frac{m^2\pi^2}{B^2}, \qquad (m = 1, 2, 3, \ldots), \quad (n = 0, 1, 2, \ldots), \tag{12.37}$$

or, alternatively,

$$\omega^2 = f^2 + gh_n\left(k^2 + \frac{m^2\pi^2}{B^2}\right) > f^2 + gh_n\frac{m^2\pi^2}{B^2} =: \omega_c^2. \tag{12.38}$$

This shows that, even though ω may continuously vary, there are quantized branches of k depending upon the horizontal (m) and vertical (n) mode structure. Obviously, for real m the elevation and the velocities across the channel are oscillatory, but depending on the value of m, the squared longitudinal wavenumber k^2 may be positive or negative, and solutions in the x-direction be oscillatory or exponential; in fact, with

$$m_{\text{crit}}^2 := \frac{B^2}{\pi^2}\frac{\omega^2 - f^2}{gh_n}, \tag{12.39}$$

one has for $m < m_{\text{crit}}$ oscillatory progressive waves and for $m > m_{\text{crit}}$ exponential variation of the fields in the x-direction.

Problem 12.4 *Using (12.1) and the solution for V, given by (12.33) and (12.34) to (12.35), show that ζ and U are given by*

$$\begin{aligned} &\zeta = \left\{\alpha_m \sin\left(\frac{m\pi y}{B}\right) - \beta_m \cos\left(\frac{m\pi y}{B}\right)\right\} \mathrm{e}^{i(kx - \omega t + \pi/2)}, \\ &\alpha_m = \phi_{mn}\frac{k}{f}\bar{V}, \qquad \beta_m = \phi_{mn}\frac{m\pi}{Bf}\frac{\omega}{f}\bar{V}, \end{aligned} \tag{12.40}$$

$$U = \left\{\bar{\alpha}_m \sin\left(\frac{m\pi y}{B}\right) - \bar{\beta}_m \cos\left(\frac{m\pi y}{B}\right)\right\} e^{i(kx-\omega t+\pi/2)},$$
$$\bar{\alpha}_m = \phi_{mn}\frac{\omega}{f}\bar{V}, \qquad \bar{\beta}_m = \frac{gh}{f}\phi_{mn}\frac{m\pi}{Bf}\frac{k}{f}\bar{V}, \tag{12.41}$$

with

$$\phi_{mn} = \frac{f^2}{\omega^2 - gh_n k^2} = \frac{f^2}{f^2 + \frac{m^2\pi^2}{B^2}gh_n}. \tag{12.42}$$

Hint*: Assume (12.40)$_1$ and (12.41)$_1$ to be correct and verify the coefficients.* ◆

The results of Problem 12.4, expressed by the formulae (12.40) and (12.41) are needed to deduce the following inferences:

- For given frequency the squared wavenumber, k^2, is only positive, provided the transverse modenumber, m is sufficiently small. Thus, for

$$m < m_{\text{crit}} := \frac{B}{\pi}\sqrt{\frac{\omega^2 - f^2}{gh_n}} \quad \rightarrow \quad k^2 > 0,$$

  the Poincaré waves are oscillatory in the x-direction. On the other hand, modes with mode number

$$m > m_{\text{crit}} \quad \rightarrow \quad k^2 < 0,$$

  are exponentially evanescent as $x \rightarrow \infty$ or $x \rightarrow -\infty$. Such waves can only exist in a semi-infinite channel or a channel of finite length. These are important in the solution of the reflection problem. This point will be taken up later again.
- Poincaré waves are necessarily *super-inertial*, i.e. their frequency ω is larger than the inertial frequency f. A fortiori, in an infinite channel (for which $k^2 > 0$) ω must be larger than the *cut-off frequency*, ω_c, whose square is the sum of f^2 and the square of the frequency of the transverse oscillation, ω_c^2, in a non-rotating channel.
- In the direction of wave progression the variable V lags behind ζ and U by $\pi/2$; so, the motion is purely transverse where U and ζ vanish and purely longitudinal where ζ experiences the largest transverse variations. This can also be inferred from Fig. 12.8a.
- The progressive Poincaré wave is asymmetric across the channel width. It possesses nodal lines of ζ where

$$\tan\left(\frac{m\pi y}{B}\right) = \frac{m\pi}{B}\frac{\omega}{k}. \tag{12.43}$$

  This equation is easily seen to have no solution for $y = B/2$. A fortiori, for the uninodal case (Fig. 12.8a, $m = 1$) the nodal line must lie in the interval $0 \leq y \leq B/2$. The asymmetry increases with decreasing ω and m and increasing

wavenumber k. In Fig. 12.8a the symmetry line is denoted by CCL and the nodal line by NL.[5]

- If the U and V components are combined to form vectors, then their vector diagram is as shown in the lower panel of Fig. 12.8a. This graph also shows an asymmetry in the velocity profile with the maximum velocities arising at the position indicated by MCL. For a stationary observer, as the wave is passing his position in the direction of wave progression, the velocity vector rotates in the *clockwise direction* in the Northern hemisphere, performing a full revolution as one wavelength passes the observer.

These properties, as well as snapshots of the elevation and velocity distributions of an uninodal ($m = 1$) and trinodal ($m = 3$) Poincaré wave are shown in Fig. 12.8, panels (a) and (b), respectively. These graphs are copied from Mortimer [27]; they are direct consequences of the formulae (12.33), (12.36)–(12.38), (12.40) and (12.41). The reader is encouraged to verify with these formulae the graphs, the figure caption and the properties spelled out in the above epitomized statements.

The structure of these solutions indicates that progressive Poincaré waves, if they exist at all in lakes (we shall provide evidence in later chapters), that they may be best measured when current meters are moored at off-shore positions. At such positions one may likely catch a strong current signal. Its clockwise rotation (on the Northern hemisphere) is then a first indication for Poincaré wave behaviour, the super-inertial frequency, $\omega > f$, being a second one.

A pseudo-standing wave pattern can also be produced along the channel, if two identical, but oppositely-propagating, Poincaré waves are combined:

$$V = V_0(y)\left\{e^{i(kx-\omega t)} + e^{-i(kx-\omega t)}\right\} = 2V_0(y)\cos(kx)e^{-i\omega t}, \qquad (12.44)$$

with $V_0(y)$ given by (12.36) and corresponding formulae for ζ and U that can easily be deduced from (12.40)–(12.42). We discuss the qualitative behaviour with the aid of Figs. 12.9 and 12.10.[6] Taking the cross-channel uninodal example from Fig. 12.8a, half-wavelength portions of two such oppositely-propagating Poincaré waves are shown in Fig. 12.9a. Eight phases in one oscillation cycle of the combined wave which they produce are numbered in sequence in Fig. 12.9b. Several features are evident: The cross channel standing wave structure is maintained, but the asymmetry, described earlier for the progressive Poincaré wave (i.e. the displacement of NL and MCL from CCL), is cancelled out: an along channel 'quasi-standing' pattern emerges, dividing the wave structure into cells; clockwise rotation of the current vectors is maintained with highest speeds at the centre of the cell; the solid boundary conditions are met at the channel sides (this is simply so by construction) but

[5] This follows from the simple fact that the equation $\tan x = c$ (=constant) has a solution x_s in the interval $[0, \pi/2]$. For growing c it is obvious (make a graph!) that x_s decreases; this is equivalent to increasing asymmetry.

[6] These beautiful figures are again redrawn from Mortimer. The discussion also parallels that of Mortimer, but is not an exact quotation.

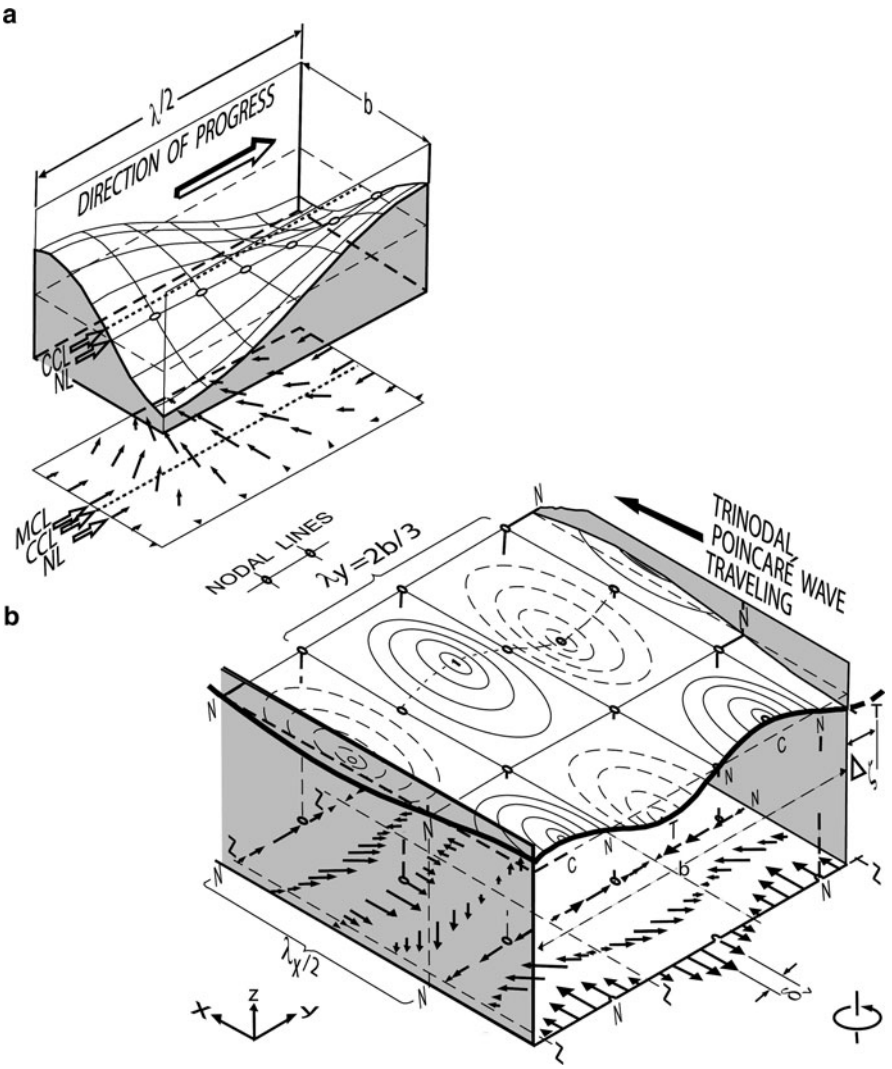

Fig. 12.8 (**a**) Progressing Poincaré wave with a uninodal ($m = 1$) cross channel distribution of the elevation ζ. Shown is a semi-period (length $\lambda/2$) with the velocity distribution in the lower *rectangle*. The *dotted line* (CCL) indicates the middle line of the channel, NL indicates the along channel nodal line shifted towards the wall to the right of the wave progression (on the Northern hemisphere); MCL marks the maximum current line. The currents along shore are sinusoidally distributed (with asymmetry) where the surface elevation shows the strongest transverse variations; it is transverse where $\zeta = 0$ across the entire channel. (**b**) Same for a trinodal progressive Poincaré wave. The nodal line of the elevation is shifted $\Delta\zeta$ to the right of the channel line, while MCL is shifted δ_v to the left of the nodal line (N) (adapted from Mortimes (1977) [27]). © Center for Great Lakes Studies (now Great Lakes WATER Institute), reproduced with permission

not at the cell ends (therefore, this is not a true standing wave, such as would be produced by a pair of oppositely-propagating plane waves in the absence of rotation); the current component in the along-shore direction at the cell end walls is small (increasingly smaller as the channel width increases) but does not fall to zero except at the centre point; the wave elevation pattern progresses clockwise around the cell-centre point (the amphidromic point P). An amphidromic point is also located at each cell corner.

Figure 12.10 illustrates four phases in one oscillation cycle of the third cross channel mode ($m = 3$) of such a pseudo-standing wave. As before, the motion has cell structure. For $t = 0$, each cell with horizontal wave lengths λ_x and λ_y is subdivided into four sub-cells in which the elevation has a high and a low, respectively, and velocities are longitudinal 'to-and-fro' as shown in the figure. A quarter period later, $t = T/4$, locations of elevation highs and lows are shifted as shown, and the current is transverse and again 'to-and-fro'. At time $t = T/2$, the elevation and velocity distributions are again as shown for $t = 0$ but with highs and lows interchanged and velocity directions reversed; a similar behaviour is seen at $t = 3T/4$ when compared with the graph for $t = T/4$. As time progresses the current vectors rotate in the clockwise direction (on the Northern hemisphere) and particle paths for a harmonic oscillation are elliptical and are traced once within a period. Finally, as before, the side boundary conditions are met, but there is no line across the channel at which the longitudinal velocity would vanish at all points for all time. Such pseudo-standing Poincaré wave solutions can therefore not hold for a closed basin.

12.5 Reflection from the End of a Channel Wall

Neither the quasi-standing Kelvin waves, see Figs. 12.3 and 12.4, nor the quasi-standing Poincaré waves, see Figs. 12.9 and 12.10, have cross channel positions at which the longitudinal velocity components would vanish at all time. So, a Kelvin wave entering a semi-infinite channel cannot be reflected at the channel end by an oppositely-propagating Kelvin wave of the same frequency. A similar statement also holds for Poincaré waves. However, it was discovered by Taylor [45] that a quasi-standing Kelvin-wave solution plus an countably infinite spectrum of reflected (backward) moving Poincaré waves allows the no-through flux condition at a transverse wall to be met.

The reflection of a Kelvin wave incident onto the end of a gulf is solved by adding to this wave a backward moving Kelvin wave of the same frequency and same wavenumber and an infinite number of backward moving, i.e. reflected Poincaré waves of the same frequency:

$$U_{\text{tot}}(x, y, \omega) = \Bigg[\left(U^{\text{in}}_{\text{Kelvin}}(x, y, \omega) + U^{\text{out}}_{\text{Kelvin}}(x, y, \omega) \right) + \sum_{m=1}^{\infty} a_m \left(U^{\text{reflected}}_{\text{Poincaré}} \right)_m (x, y, \omega) \Bigg]. \tag{12.45}$$

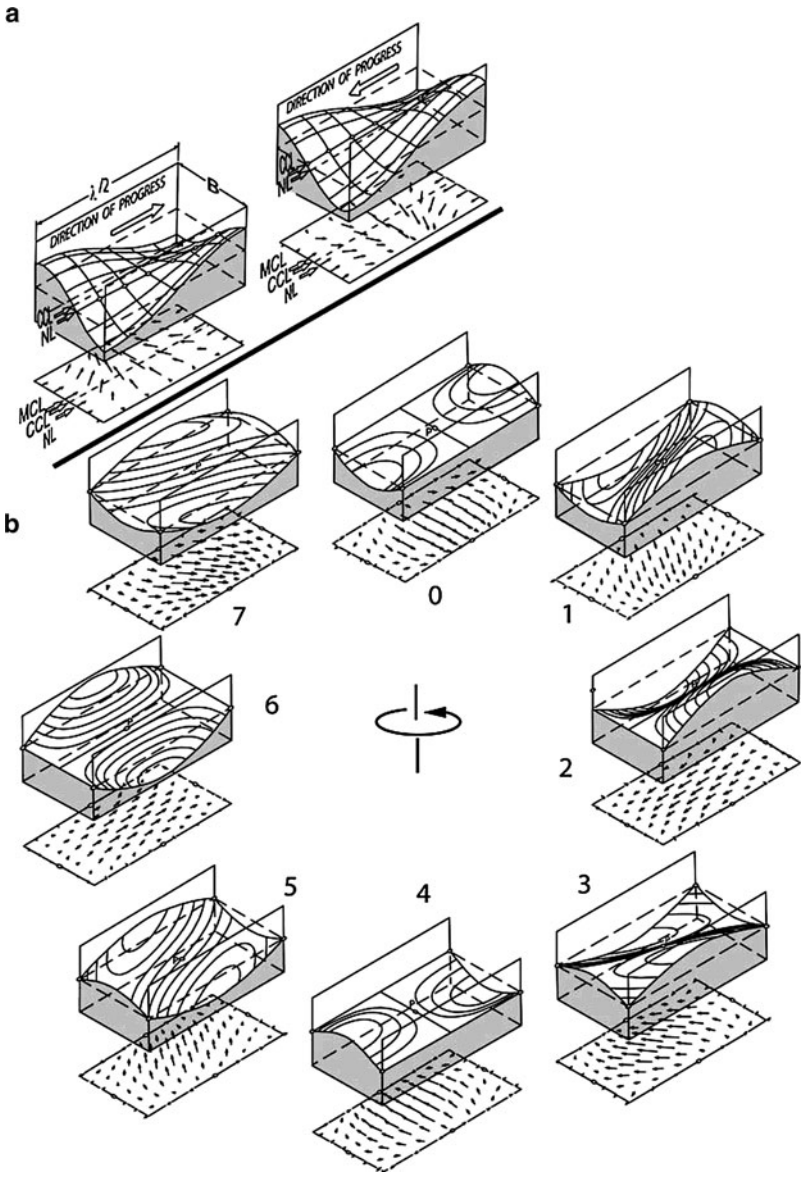

Fig. 12.9 Two oppositely-propagating but otherwise identical progressive Poincaré waves, from Fig. 12.8a and shown here in (**a**), combine to produce the amphidromic 'standing' Poincaré wave. Half-wavelength cells of the combined pseudo-standing wave are illustrated at 1/8-cycle intervals in (**b**). The combined wave, with amphidromic point P at the cell-centre, is truly standing (with one node in this case) across, but quasi-standing along the channel, as explained in the text. Wave topography can be viewed either as that of a water surface or as that of a 'thermocline' interface in a two-layered model, in which case the horizontal current vectors (illustrated beneath each cell) are those in the lower layer (adapted from Mortimer (1977) [26]). © Center for Great Lakes Studies (now Great Lakes WATER Institute), reproduced with permission

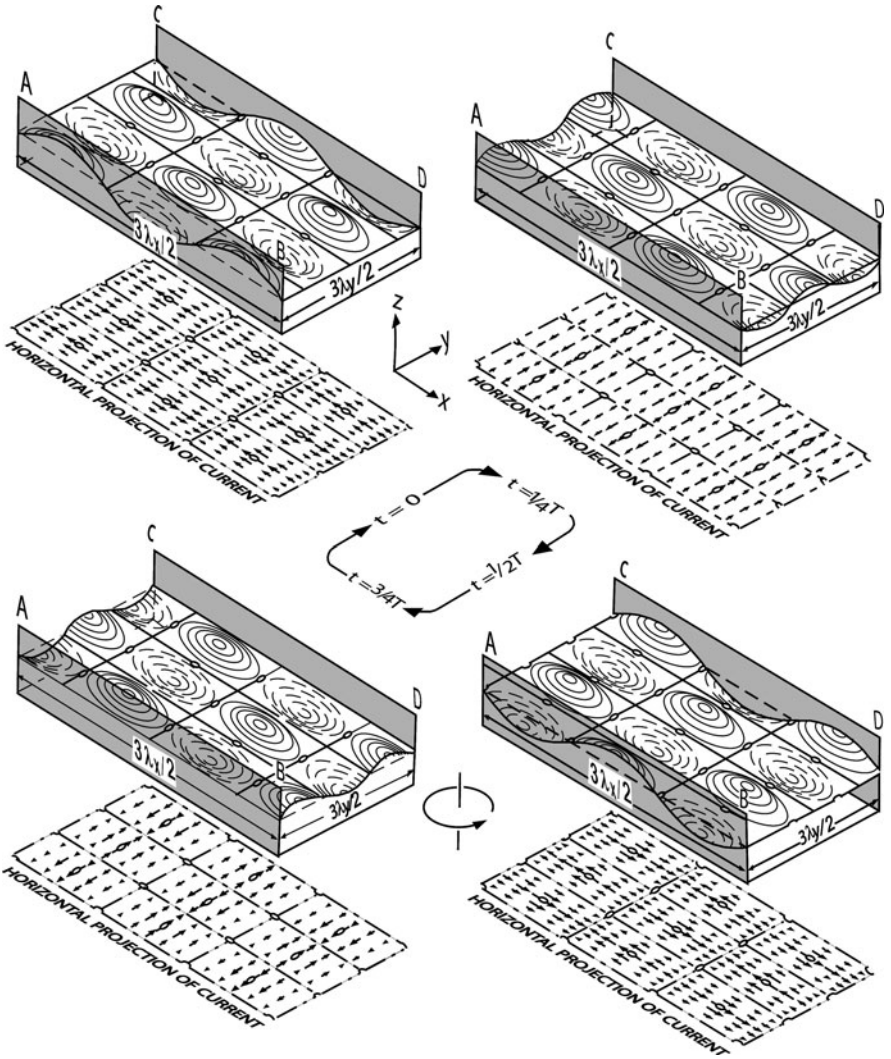

Fig. 12.10 A 'standing' Poincaré wave of cross-channel nodality 3, i.e. a trinodal equivalent of Fig. 12.9b, but with only 4 phases of the oscillation cycle shown. The same legend as for Fig. 12.9 applies; and the progressive Poincaré wave component, contributing to this combination, is illustrated in Fig. 12.9 (lower part) (adapted from Mortimer (1980) [27]). © Center for Great Lakes Studies (now Great Lakes WATER Institute), reproduced with permission

The free amplitudes, a_m, of these Poincaré waves are determined by the condition that there is no-flux through the channel wall:

$$U_{\text{tot}}(x_{\text{wall}}, y, \omega) = 0, \qquad y \in [0, B]. \tag{12.46}$$

in which the amplitude of $U^{\text{in}}_{\text{Kelvin}}$ is explicitly known. Before this equation can be exploited, the functions $U^{\text{in}}_{\text{Kelvin}}(x_{\text{wall}}, y, \omega)$ and $U^{\text{out}}_{\text{Kelvin}}(x_{\text{wall}}, y, \omega)$, which

are exponentials, must be expanded in Fourier-sine series with the elements $\sin(m\pi y/B)$, which describe the transverse variability of the functions $(U^{\text{reflected}}_{\text{Poincaré}})_m$, $m = 1, \ldots, \infty$. This then makes the right-hand side of (12.45) an infinite linear combination of $\sin(m\pi y/B)$, $m = 1, \ldots, \infty$, that must be zero. This yields an infinite number of equations for the coefficients a_m. By truncating the number of quasi-standing Poincaré modes to $m = 1, 2, \ldots, M < \infty$, the problem of the reflection of a Kelvin wave at the end of a gulf can explicitly be solved. This has been done by Taylor in 1920 [45], see Fig. 12.11.

If the incoming Kelvin wave has a frequency below the cut-off frequency, ω_c, of Poincaré waves, then the Poincaré modes are all evanescent as one moves away from the end wall. Although they are important for the satisfaction of the boundary condition, their presence is felt only near the end wall. For this reason, this type of reflection is called *complete reflection*. Figure 12.12 shows the amphidromic system and the current ellipses in a rectangular basin closed at one end as determined by Taylor.[7] The influence of the Poincaré waves is only seen near the channel end. When the frequency of the incoming wave is above the cut-off frequency, then this incoming Kelvin wave is reflected by a backward moving Kelvin wave and a finite number of reflected Poincaré waves, of which the presence is recognized in the *entire* basin, plus an infinite number of Poincaré waves, which are exponentially evanescent. Reflections are then called *incomplete*.

An example of the amphidrome modification near the closed end is shown for this case in Fig. 12.13 for higher frequencies, the amplitude pattern diverges from that due to a pair of Kelvin waves, acquiring more and more lateral structure as more and more Poincaré modes are reflected from the closed end of the channel. Figure 12.13, taken from [2] shows the distortion of the amphidromes with increasing frequencies.

12.6 Shallow Water Waves in a Rectangle of Constant Depth

The above description also makes clear, in principle, how quasi-standing shallow water waves can be treated in a (alongated) rectangular basin of constant depth. The longitudinal velocity U could be composed of a pair of a forward and backward moving Kelvin waves plus two infinite sums of Poincaré waves, of which one set is reflected at the front wall, $x = x_{\text{front}}$, the other at the back wall, $x = x_{\text{back}}$. Consequently,

$$U_{\text{tot}}(x, y, \omega) = U^{\text{forward}}_{\text{Kelvin}}(x, y, \omega) + U^{\text{backward}}_{\text{Kelvin}}(x, y, \omega) + \sum_{m=1}^{\infty} a_m \left(U^{\text{reflected}}_{\text{Poincaré}}\right)^{\text{front}}_m + \sum_{m=1}^{\infty} b_m \left(U^{\text{reflected}}_{\text{Poincaré}}\right)^{\text{back}}_m \tag{12.47}$$

[7] For a biographical sketch see Fig. 12.11.

Fig. 12.11 Geoffrey Ingram Taylor (1886–1975) (portrait from http://en.wikipedia.org/) and wavy Taylor vortices in the gap between concentrical cylinders, reproduced in laboratory (photo: K.G. Roesner, http://www.kgroesner.de/).

Geoffrey Ingram Taylor (7 March 1886, St. John's Wood, London; 27 June 1975, Cambridge, England) was an applied mathematician and physicist specialized in fluid dynamics and wave theory. His father was an artist, and his mother, Margaret Boole, came from a family of mathematicians. Taylor followed her footsteps studying mathematics at Trinity College, Cambridge University. With work on shock waves, 1909, he won the Smith's Prize and was elected a fellow at Trinity College in 1910 and a Reader in Dynamical Meteorology in the following year. His publication 'Turbulent motion in fluids' won him the Adams Prize in 1915.

During World War II Taylor was sent to the Royal Aircraft Factory in Farnborough to apply his knowledge in aerodynamics and meteorology to aircraft design; there he worked on stress in propeller shafts, learned to fly airplanes and made parachute jumps. After World War I, he returned to Cambridge, where he worked on rotating fluids. It is at this time when his paper on the reflection of a Kelvin wave at the end of a gulf with rectangular cross-section was written, which required a combination of the incoming Kelvin wave with an outgoing Kelvin wave and an infinite number of Poincaré waves. In 1915, Taylor was appointed a Royal Society research professorship. This freed him from teaching and led to a period of very active research on both fluid and solid mechanics (also of crystalline materials), including statistical approaches to turbulence. In 1934, Taylor realized – almost simultaneously with Polanyi and Orovan – that the plastic deformation of ductile material could be explained with the theory of dislocations.

During World War II Taylor worked on applications of his expertise to military problems, among others the propagation of blast waves in air and water. His prediction of the strength of the atomic explosion performed as part of the Manhattan Project in the desert of New Mexico is well known. In 1944, he was also knighted.

Taylor continued his research after the war, working on the development of supersonic aircraft. He officially retired in 1952 from active duty; he continued to work for twenty more years. He wrote his final paper on electrical activity in thunderstorms in 1969, when he was 83. He suffered a stroke in 1972 and died on 27 June 1975.

The text is based on: http://en.wikipedia.org/wiki/Geoffrey-Ingram_Taylor

Further references:

B. Pippard: Sir Geoffrey Taylor, Physics Today, Sept 1975, p 67
G. Batchelor. The life and legacy of G.I. Taylor. Cambridge University Press, 1994. ISBN 0-521-46121-9.

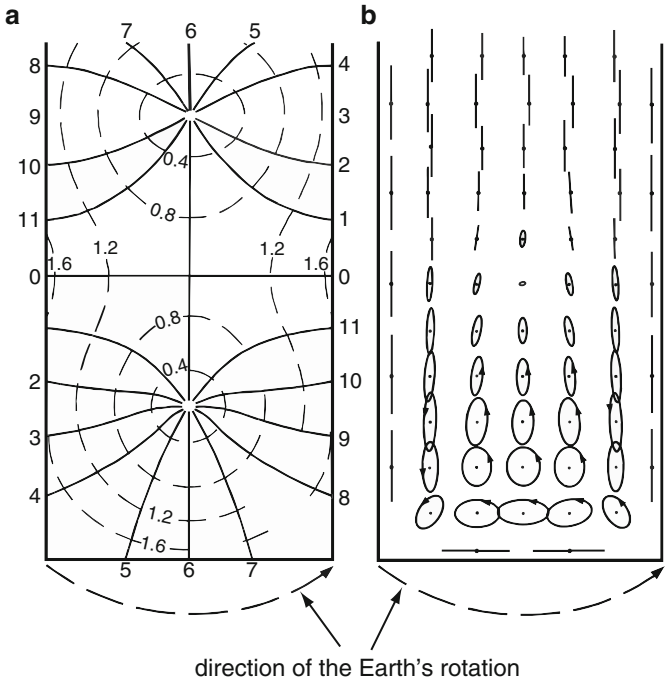

Fig. 12.12 Amphidromic system in a rectangular basin closed at one end. (**a**) co-tidal and co-range lines; (**b**) current ellipses, illustrating pure reflection. The *arrow* at the *bottom* indicates the rotation of the Earth, after G.I. Taylor [45] (1920). © London Mathematical Society, reproduced with permission

must hold, subject to the reflection conditions

$$U_{\text{tot}}(x_{\text{front}}, y, \omega) = 0, \qquad U_{\text{tot}}(x_{\text{back}}, y, \omega) = 0. \tag{12.48}$$

In addition, the periodicity condition

$$|x_{\text{back}} - x_{\text{front}}| = p\pi \qquad (p = 1, 2, \dots)$$

must hold. This defines the dispersion relation and hence the frequencies which are now quantized and isolated.

Upon Fourier expansion of $U_{\text{Kelvin}}^{\text{forward}}(x, y, \omega)$ and $U_{\text{Kelvin}}^{\text{backward}}(x, y, \omega)$ in y at $x = x_{\text{front}}$ and $x = x_{\text{back}}$, equations (12.48) form a linear homogeneous set of $2M$ ($M \to \infty$) equations for the amplitude coefficients a_m and b_m ($m = 1, \dots, M$). Setting the determinant of this system of equations equal to zero guarantees non-trivial solutions and determines the eigenfrequencies ω_{mp}, which are now quantized and isolated (m gives the mode number in the y-direction, p that in the x-direction). The eigenfrequencies carry three integer indices ω_{nmp}, $n = 0, 1, 2, \dots$ to identify

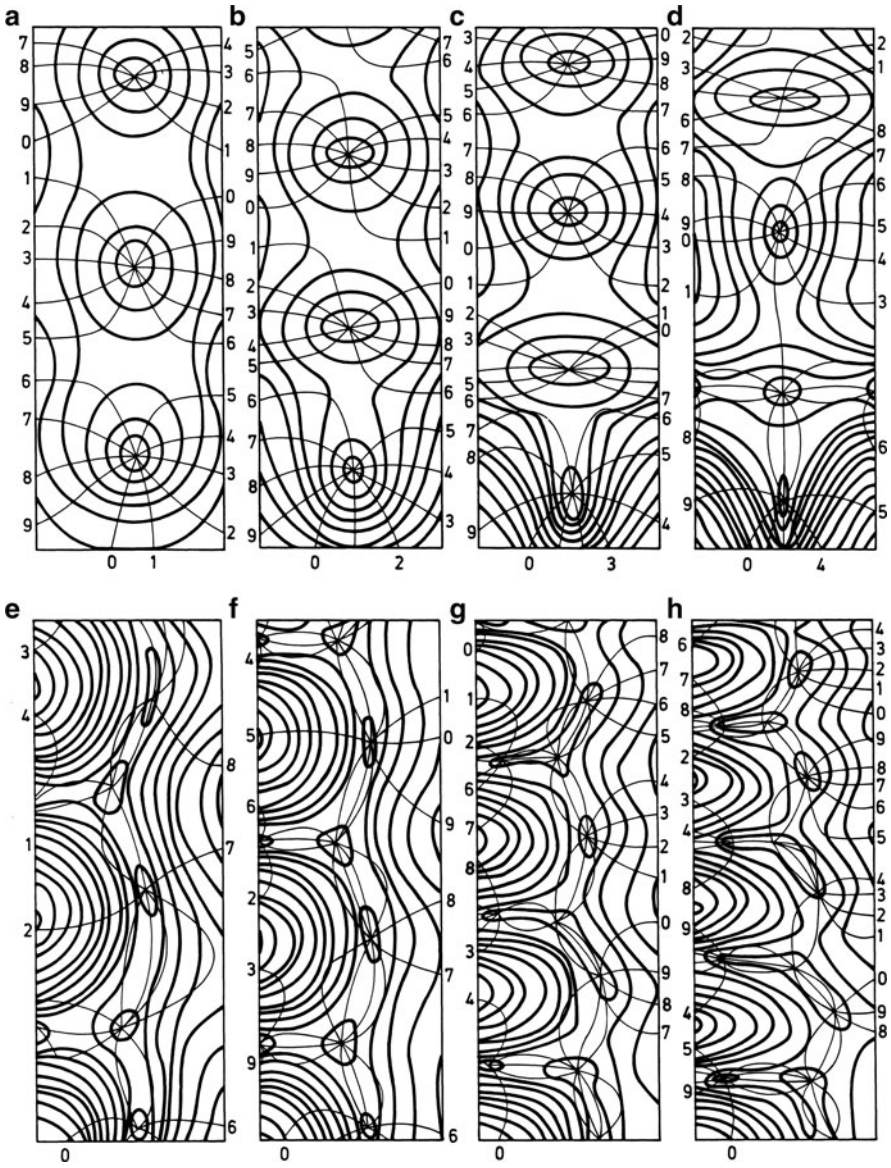

Fig. 12.13 Influence of the frequency on the amphidromic pattern for Kelvin waves reflected from the closed end of a channel. The closed end of the channel is at the *bottom* of the panels, and lines of constant phase and amplitude are labeled as *thin* and *heavy solid lines*. The width of the channel is $B = 500\,\mathrm{km}$, the latitude 54.46°N and the cut-off period is $T_c = 2\pi/\omega_c$ is equal to 8.46 h for $m = 1$. The Kelvin wave period decreases from panels (**a**)–(**h**) as follows: (**a**): 12.0 h; (**b**): 10.0 h; (**c**): 9.0 h; (**d**): 8.6 h; (**e**): 8.1 h; (**f**): 8.0 h; (**g**): 7.0 h; (**h**): 6.0 h. In panels (**a**)–(**d**), all Poincaré waves are evanescent, and at sufficiently large distance from the reflecting end the interference pattern becomes that of a pair of Kelvin waves travelling in opposite directions. In the last four panels (**e**)–(**h**), the $m = 1$ Poincaré mode propagates and the field far from the reflecting end consists of two Kelvin waves and a Poincaré wave. The asymmetry introduced by the reflected Poincaré wave is evident in the four panels (adapted from Brown (1973) [2]). © J. Marine Research, reproduced with permission

the barotropic vertical mode, and an infinity of baroclinic vertical modes, $m = 1, 2, 3, \ldots$ to identify the transverse and $p = 1, 2, 3, \ldots$ the longitudinal basin-scale modes.

Of course, such a solution technique is complicated for practical applications. But it is at least helpful to physically interpret free wave dynamics in oblong basins, strictly only for a homogeneous fluid in a rectangular basin. If this rectangle is long, then the eigenfrequency is below the cut-off frequency, at least for some of the lowest order modes. The quasi-standing Kelvin waves at these frequencies are complemented by Poincaré waves that are reflected at the two end cross sections and are evanescent as one moves away from these cross sections into the interior of the basin. These waves can be termed *Kelvin-like*, because 'Poincaré-type perturbations' are only appreciably excited at the long ends. Any eigenfrequency above the cut-off frequency $\omega_{mp} > \omega_c$ will generate Poincaré solutions which are oscillatory throughout the basin. Current measurements at off-shore moorings will most likely have the potential to record these Poincaré-type solutions. For more compact rectangles, say squares, the mode structure generally fills the entire rectangle and Kelvin- and Poincaré-type wave forms are intermixed.

12.6.1 Frequency Relation

The mathematical construction of eigensolutions for homogeneous water in rotating rectangles of constant depth has a relatively long history beginning with Lord Rayleigh [41, 42] and culminating with the doctoral dissertation by Rao [39] and its condensed version 'Free gravity oscillations in rotating rectangular basins', published in the Journal of Fluid Mechanics [40]. Rao writes: "Rayleigh's treatment was restricted to the case where the rotation speed[8] Ω was small compared with the speed ω of the oscillation and was later corrected by Proudman [34]. Taylor [45] gave the first complete solution (valid for any Ω) for the free oscillations in a rectangular basin. Some of his conclusions were criticized by Jeffreys [11], who pointed out that there was a double infinity of modes in the rotating case and that there might be modes travelling in both directions of the basin (with and against the rotation [Ω]). Defant [8] subsequently gave an approximate method of simplifying Taylor's analysis.

Lamb [16] gave an approximation to the slowest speed by a different method. His result is

$$(\omega^2 - \nu_1^2)(\omega^2 - \nu_2^2) = \left(\frac{4}{\pi}\right)^4 \Omega^2 \omega^2, \tag{12.49}$$

where ν_1 and ν_2 are the speeds of the slowest longitudinal and slowest transverse modes in the zero-rotation case (see, Chap. 7, Sect. 7.3 in Volume I).[9] In the special

[8] Rao calls 'angular velocity' 'rotation speed' or simply 'speed'.

[9] The frequency ν_j in the zero-rotation limit, $\Omega = 0$, is

case of a square, $\nu_1 = \nu_2$, and (12.49) reduces to

$$\omega - \nu_1 = \pm \frac{8}{\pi^2} \Omega. \tag{12.50}$$

This agrees with the result of Rayleigh [41] as corrected by Proudman [34].[10] Lamb also showed that there are wave systems travelling in both directions around the basin. Goldsbrough [10] solved the problem formally for any Ω, but approximated results to small Ω. He confirmed Lamb's results.

Corkan and Doodson [7] treated the case of a square sea by direct numerical integration of the dynamic equations and obtained frequency values at a few rotation speeds for the slowest positively (in the same direction as the rotation) and negatively (opposite the direction of rotation) propagating anti-symmetric modes. [...]. They found that negative waves are 'unstable' in the sense that these waves are transformed into positive waves at high rotations.

[...] Van Danzig and Lauwerier [46] [...] obtained a solution valid for any Ω but approximated the results to small values of Ω. The explicit results obtained by them are

$$\frac{\omega}{\nu_1} = 1 \pm \left(\frac{4}{\pi^2}\right) \frac{2\Omega}{\nu_1} + 0.138 \left(\frac{2\Omega}{\nu_1}\right)^2 + \cdots \tag{12.53}$$

for a square. The minus sign refers to the slowest positive anti-symmetric mode and the plus sign to the negative mode. This extends the approximation (12.50) of Lamb and Rayleigh by one more order in Ω. For a (2×1)-rectangle Van␣Danzig and Lauwerier give an explicit result only for the lowest order in Ω for the slowest positive anti-symmetric mode

$$\nu_{kl} = \pi \left\{ \left[(k/a)^2 + (l/b)^2 \right] g h_n \right\}^{1/2}, \quad \nu_1 := \min_{(k,l)} \nu_{kl},$$

where a and b are the side lengths of the rectangle. For $a > b$, ν_1 is obtained for $(k, l) = (1, 0)$; g is the acceleration due to gravity and h_n the equivalent depth for barotropic ($h_n = H$) or baroclinc modes.

[10] Rao is not very precise here. The result (12.50) is an approximation to (12.49) if $\nu_1 = \nu_2$. Indeed, for $\nu_1 = \nu_2$, (12.49) becomes

$$(\omega^2 - \nu_1^2) = \pm (\tfrac{4}{\pi})^2 \Omega \omega, \tag{12.51}$$

which, for $\Omega \to 0$ allows construction of the iterative solution

$$\omega_n = \nu_1 \sqrt{1 \pm (\tfrac{4}{\pi})^2 \tfrac{\Omega \omega_{n-1}}{\nu_1^2}}$$

with the first two iterates

$$\omega_0 = \nu_1, \quad \omega_1 = \nu_1 \sqrt{1 \pm (\tfrac{4}{\pi})^2 \tfrac{\Omega}{\nu_1}} \sim \nu_1 \pm \tfrac{8}{\pi^2} \Omega. \tag{12.52}$$

Lamb [17] (1932, p. 313, (22)) writes that (12.52) is approximate for $\Omega \to 0$.

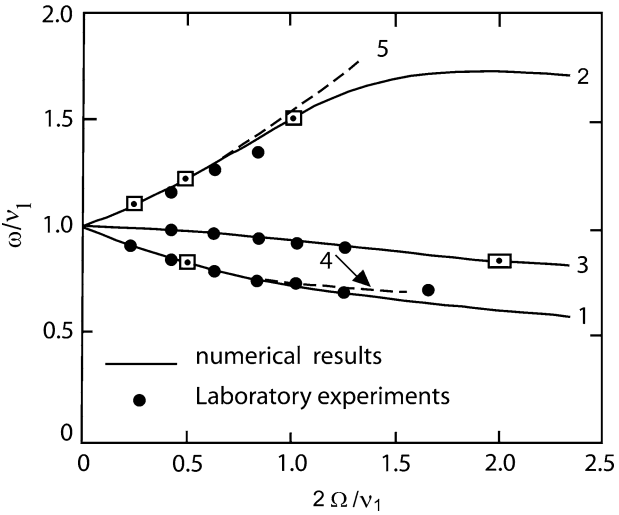

Fig. 12.14 Dimensionless frequency of oscillation (ω/ν_1) in *square* and *rectangular* basins of uniform depth, as a function of the dimensionless rotation speed ($2\,\Omega/\nu_1$). The *solid curves* are the results of Rao [40]: curves 1 and 2 correspond to the slowest positive and negative modes in a square and curve 3 to the slowest positive mode in a (2 × 1)-rectangle. Also shown are Corkan and Doodson's [7] results for the *square* (⊡) and Taylor's [45] results for a (2 × 1)-rectangle (⊡). Curves 4 and 5 show the results of Van Danzig and Lauwerier's [46] perturbation analysis for the slowest positive and negative modes in a square, valid to second order terms in ($2\,\Omega/\nu_1$). *Full circles* are obtained from laboratory experiments. The figure is a combination of two figures by Rao [40]. © J. Fluid Mech. Cambridge University Press, reproduced with permission

$$\frac{\omega}{\nu_1} = 1 - 0.302\left(\frac{2\Omega}{\nu_1}\right)^2, \tag{12.54}$$

which agrees with the result of Rayleigh [42] as corrected by Proudman [34], when specialized to the case of a (2 × 1)-rectangle", [40].

This is Rao's summary of the history of the problem prior to his work. He [40] determined the eigenfrequencies of the gravitational oscillations of a homogeneous fluid in a rectangle for any value of the rotation frequency. He conducted computations for the frequencies and modal structures of several of the lowest symmetric and anti-symmetric modes in a square and a (2 × 1)-rectangle. Figure 12.14 is a combined reproduction of two of his figures showing the frequency results for the slowest positive and negative modes in a square and the slowest positive anti-symmetric mode in a (2 × 1)-rectangle. In this diagram, the frequencies ω and Ω are non-dimensionalized by ν_1, the slowest zero-rotation frequency. For detailed explanations we refer to the figure caption.

Rao also determined the modal frequencies for other modes higher than those shown in Fig. 12.14. A number of these are shown in Fig. 12.15 for squares on the left and (2 × 1)-rectangles on the right. 'This diagram exhibits the effect of rotation on all modes of the zero-rotation spectrum with frequencies in the range $\omega/\nu_1 < 4$

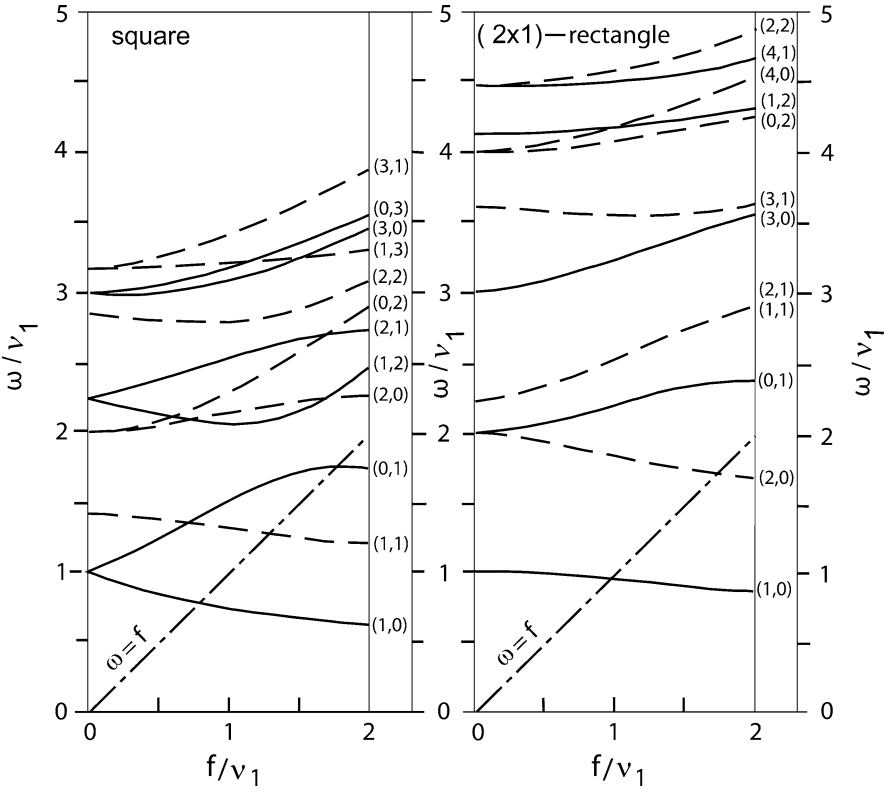

Fig. 12.15 Frequency (ω/ν_1) vs. rotation speed (f/ν_1) ($f = 2\,\Omega \sin\phi$) for various modes in a *square* (*left*) and (2×1)-rectangular (*right*) basin. *Solid* (*dashed*) *lines* correspond to anti-symmetric (symmetric) modes. Modes are identified by (k, l). For *squares*, in the non-rotation limit, some are doubly valued. The *dashed-dotted lines* separate the regimes of sub- and super-inertial frequencies (redrawn from [40]). © J. Fluid Mech. Cambridge University Press, reproduced with permission

for the square and $\omega/\nu_1 < 5$ for the rectangle. The solid lines correspond to anti-symmetric modes and the dashed lines to symmetric modes. The slowest mode of all is the anti-symmetric mode $(1, 0)$ which consists of one wave travelling in the positive direction of the basin; that is, in the same direction as that of rotation' [40]. The figure shows the $[(1, 0), (0, 1)]$, $[(1, 2), (2, 1)]$, $[(3, 0), (0, 3)]$ modes in a square; these are examples of doublets in the zero-rotation frequency spectrum for anti-symmetric modes. Similarly, the $[(2, 0), (0, 2)]$, $[(1, 3), (3, 1)]$ modes in a square are such doublets for anti-symmetric modes. These multiplets in the zero-rotation spectrum are split into distinct frequencies on the introduction of rotation. For the modes of the (2×1)-rectangle the zero-rotation limits of the frequencies are, however, all singlets. Moreover, note that square and (2×1)-rectangle have certain modes whose eigenfrequencies are sub-inertial ($\omega < f$) if the rotation speed Ω is sufficiently

large. Most frequencies are, however, super-inertial. Rao also demonstrates that with increasing aspect ratio of the rectangle

- The effect of the rotation on the frequencies of the few lowest longitudinal oscillations becomes less important and in the limit as $a/b \to \infty$, these oscillations are transformed into Kelvin waves,
- Purely transverse modes assume the form of waves with horizontal crests and, thus, approach in the limit as $a/b \to \infty$ Sverdrup waves, for which $\omega^2 = \nu^2 + f^2$.

12.6.2 Modal Structure

The elevation field of the free surface (or the displacement in an equivalent depth model) ζ may be written as

$$\zeta(x, y, t) = A(x, y) \cos[\omega t - \theta(x, y)]. \tag{12.55}$$

Here, $A(x, y)$ is the amplitude and $\theta(x, y)$ is the phase of high water at a point (x, y). Graphical representations of the modal structure are usually given in terms of co-amplitude lines (contours of A) and co-tidal lines (contours of θ) with a particular normalization of the amplitude function. Rao put the average value of A^2 over the basin equal to 100 in all cases. (It is generally more customary in practice to set the maximum value of A equal to 100.) In Figs. 12.16–12.19, the co-tidal lines are drawn at one-twelfth period, i.e. in θ-increments of 30° through the range $0 \leq \theta \leq 360°$. In what follows, we take $\Omega > 0$, that is the rotation of the basin is positive (on the Northern hemisphere, counterclockwise) and each figure shows results for a square and for a (2×1)-rectangle.

"The slowest positively propagating mode $(1, 0)$ is presented in Fig. 12.16, for rotation speed $f/\nu_1 = 2$. This mode, in both basins, consists of one wave travelling in the positive (counter-clockwise) direction about an amphidromic point at the centre of the basin. The amplitude of oscillation is zero at the amphidromic point and increases outward; it reaches a maximum value at the corners. This structure of the mode remains essentially unchanged with increasing rotation. In the sequel we refer to an amphidromic point as positive or negative according as the associated wave system rotates in the positive (counter-clockwise) or negative (clockwise sense). Open circles represent positive amphidromes, full circles will identify negative amphidromes.

Figure 12.17a–c represent the slowest negative mode at different values of f/ν_1 (note they are not the same for squares and (2×1)-rectangles). Taking first the case of a square, we see that for low rotation this mode consists of one wave travelling in the clockwise direction about an amphidromic point at the centre of the basin, as shown in Fig. 12.17a. As the rotation increases, the structure of the mode changes, in marked contrast to the slowest positive mode. In particular, for a certain value of f/ν_1, (not precisely determined [...] but in the range $1.0 < f/\nu_1 < 1.1$) a

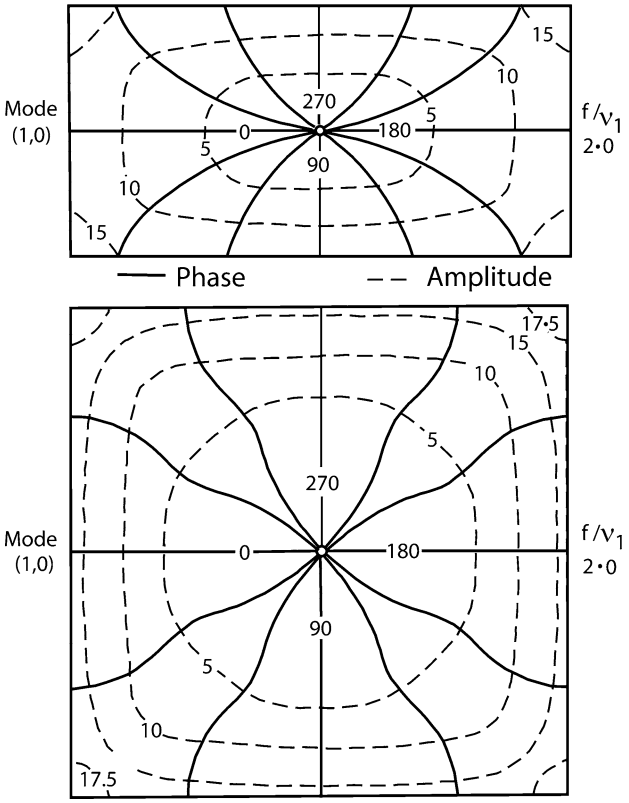

Fig. 12.16 Structure of the slowest positive amphidromic mode in a (2 × 1)-rectangle and in a *square*. In this and the following diagrams, *open circles* represent a positive amphidromic point, whilst *full circles* represent a negative amphidromic system (redrawn from [40]). © J. Fluid Mech. Cambridge University Press, reproduced with permission

system of four amphidromic points enters the basin from the boundaries as shown in Fig. 12.17b. As the rotation increases, these points move towards the centre of the basin, and the positive wave systems associated with them eventually dominate over the central negative wave. Even though there are five amphidromic points, the arrangement is such that the central negative-wave region is surrounded by a system of three waves which travel around the boundaries in a positive direction, as can be seen by careful examination of the co-tidal lines of Fig. 12.17b. As the rotation increases, the inner negative wave region contracts and the amplitude of this wave decreases. At $f/\nu_1 = 1.5$ (Fig. 12.17c) the amplitude of the negative wave is practically zero [...].

The upper parts of Fig. 12.17a–c show the slowest amphidromic mode in a (2 × 1)-rectangle. In this case, even at the low rotation $f/\nu_1 = 0.1$, there is one negative wave system (Fig. 12.17a) at the centre of the basin and two positive wave systems with amphidromic points located one on either side of the centre

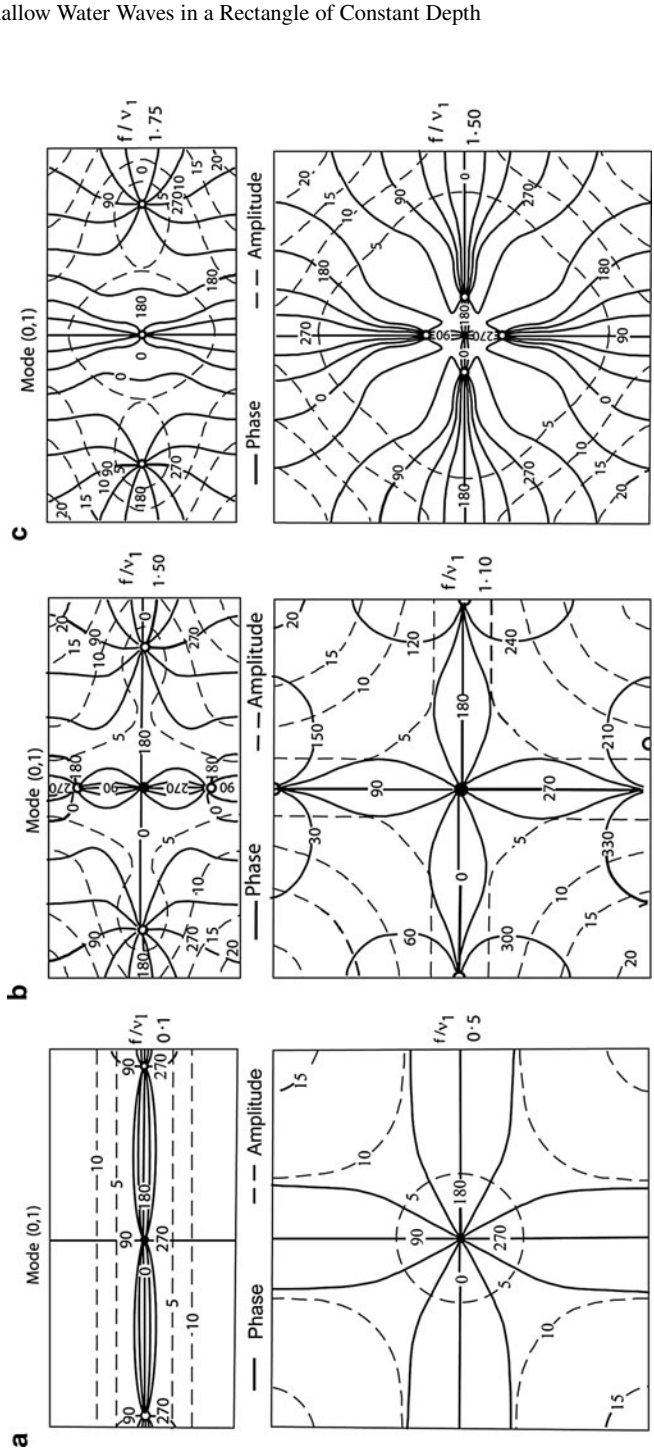

Fig. 12.17 The slowest negative anti-symmetric mode (0, 1) at the rotation speed $f/\nu_1 = (0.5, 0.1)$ (**a**), $f/\nu_1 = (1.10, 1.50)$ (**b**) and $f/\nu_1 = (1.50, 1.75)$ (**c**), for a *square* and (2×1)-rectangle, respectively (redrawn from [40]). © J. Fluid Mech. Cambridge University Press, reproduced with permission

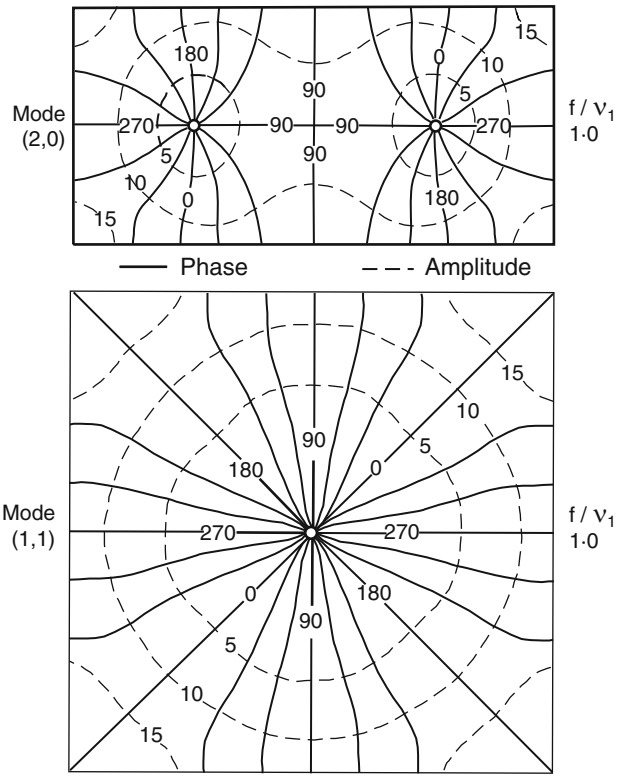

Fig. 12.18 The slowest positive symmetric mode for a *square* and a (2×1) – real angle and $f/\nu_1 = 1.0$ (redrawn from [40]). © J. Fluid Mech. Cambridge University Press, reproduced with permission

of the longitudinal axis. As the rotation is increased (Fig. 12.17b), two more positive amphidromic systems enter the basin, one on either side of the centre on the transversal axis, for a value of f/ν_1 in the range $1.4 < f/\nu_1 < 1.5$. Finally, by $f/\nu_1 = 1.75$ (Fig. 12.17c) the central negative amphidromic system disappears and one has three positive waves in the basin with amphidromic points located on the longitudinal axis" [40].

Next, consider the symmetric modes. In Fig. 12.18, we have displayed the slowest positive modes belonging to this family in a square and a (2×1)-rectangle for $f/\nu_1 = 1.0$. "The system consists of two waves travelling in the positive direction and the structure remains unchanged with increasing rotation. In the square, both waves travel around an amphidromic point at the centre of the basin, whereas in the (2×1)-rectangle, each wave has a separate amphidromic point located symmetrically with respect to the centre on the longitudinal axis. At $f/\nu_1 = 1.0$, Fig. 12.19a shows that the corresponding negatively propagating modes also consist of two waves. Just as [for] the first negative anti-symmetric mode, these modes undergo a

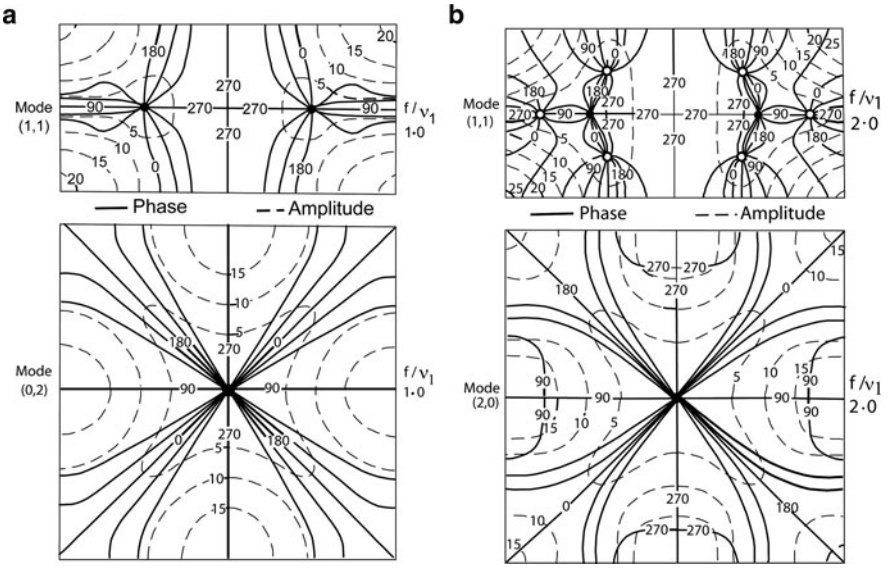

Fig. 12.19 The slowest negative symmetric mode at the rotation speeds $f/\nu_1 = 1.0$ (**a**) and $f/\nu_1 = 2.0$ (**b**) (redrawn from [40]). © J. Fluid Mech. Cambridge University Press, reproduced with permission

change in structure with increase in rotation: positive amphidromic points external to the basin gradually move across the boundary into the basin. The situation when $f/\nu_1 = 2.0$ is shown in Fig. 12.19b" [40].

The higher modes become very complicated in their structure, so we refrain from presenting them in any detail here, except to mention that negative amphidromic systems always appear to be 'unstable', that is, to give way to positive amphidromic systems.

12.6.3 Additional Results

Rao [40] also demonstrated that in long rectangles the determination of the (1, 0)-amphidromic system by 'Kelvin-wave dynamics' is a good approximation to the exact solution, see Problem 12.1. The surface displacement can be written as shown in (12.55) with

$$A(x,y) \equiv \left[\cos^2\left(\frac{\pi x}{a}\right) + \frac{f^2}{gh_n}\left(y - \frac{b}{2}\right)^2 \sin^2\left(\frac{\pi x}{a}\right)\right]^{1/2},$$
$$\theta(x,y) \equiv \arctan\left[\frac{f}{gh_n}\left(y - \frac{b}{2}\right)\tan\left(\frac{\pi x}{a}\right)\right]. \tag{12.56}$$

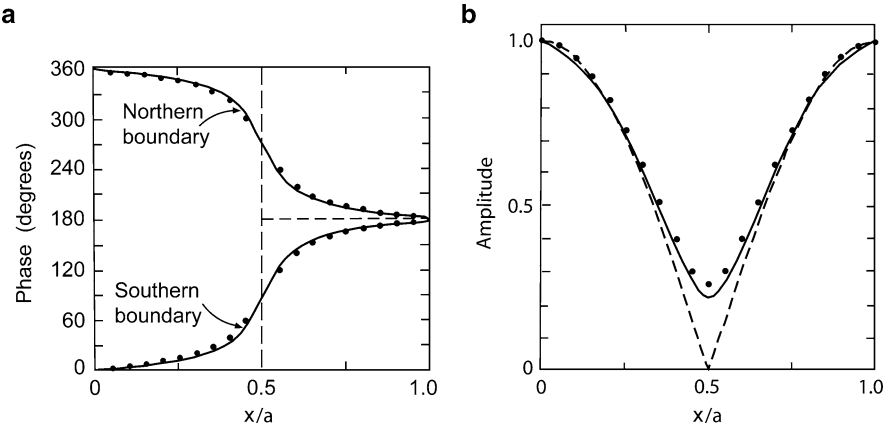

Fig. 12.20 Amplitude (**a**) and phase of high water (**b**) for the slowest longitudinal oscillation on the boundaries of a (6×1)-rectangular basin with rotation speed $f/\nu_1 = 1$. The *solid line* is the exact calculation, the *dots* are the results of applying the Kelvin-wave hypothesis and the *dashed line* is the situation with zero rotation (redrawn from two figures of [40]). © J. Fluid Mech. Cambridge University Press, reproduced with permission

Rao [40] plotted the amplitudes and phases of high water along the North and South boundaries (parallel to the x-axis) of the basin obtained from the exact analysis of the problem and from the above Kelvin-wave approximation for a (6×1)-rectangle with a rotation speed $f/\nu_1 = 1.0$, see Fig. 12.20. The figure also shows the situation in the non-rotating case. It provides ample demonstration of the accuracy of the approximate solution obtained by Kelvin-wave dynamics.

Rao also presented an analysis of the energy partition. In the zero-rotation case, the total energy is partitioned equally between potential and kinetic energy (i.e. the integrals of these energy densities over the rectangle and over a time period are the same. The motion is in this case irrotational. In the rotating case, the kinetic energy of the motion is resolved into two additive contributions due to irrotational and rotational motion, and the equipartition property is lost.

Rao also performed laboratory experiments with a rotating square tank of dimensions $a = b = 48.69\,\text{cm}$ and a water depth $H = 0.125\,a$. Distilled water was used with an organic tracer of 10^{-3} concentration added to reduce surface tension. Rao measured upper and lower bounds for the frequency (ω/ν) at rotation speeds of the tank $\Omega = 0, 0.5, 1.0, \ldots, 4.0\,\text{rad}\,\text{s}^{-1}$. The full circles in Fig. 12.20 are the results for the slowest negative anti-symmetric mode $(1, 0)$, the slowest positive anti-symmetric mode $(0, 1)$ and the slowest positive symmetric mode $(1, 1)$. Agreement between the experimental and the theoretical frequency is very good; 'the maximum error obtained is 6% for the $(1, 0)$ mode at $\Omega = 4\,\text{rad}\,\text{s}^{-1}$. However, at this speed of rotation the free surface assumes a very pronounced parabolic shape, and it is not surprising that results of the planar theory (which ignores the free surface curvature) do not (in this case) agree well with experimental results'.

It may, further, be mentioned that the solutions for the gravitational oscillations of a homogeneous fluid in a rectangular basin of constant depth have been numerically determined by Rao [39] by a method, originally designed by Proudman [33]. The method is to additively decompose the horizontal transport vector $\boldsymbol{V}$ into two contributions, $\boldsymbol{V} = \boldsymbol{V}^{\phi} + \boldsymbol{V}^{\psi}$, such that $\boldsymbol{V}^{\phi} = -\nabla\phi$ is irrotational and $\boldsymbol{V}^{\psi} = h^{-1}\boldsymbol{k} \times \nabla\psi$, is solenoidal. (Here, $\boldsymbol{k}$ is a unit normal vector pointing into the z-direction and $h = H/\bar{H}$ is the non-dimensional ratio of the actual depth H and the basin mean depth). Two selfadjoint boundary value problems for the potential ϕ and the stream function ψ then define function sets $\{\phi_\alpha\}$ and $\{\psi_\alpha\}$ ($\alpha = 1, 2, \ldots, \infty$) which satisfy the no-flux condition through the boundary, are complete in the set of square integrable functions and can be used to define expansions for $\boldsymbol{V}^{\phi}$, $\boldsymbol{V}^{\psi}$ and ζ. The governing equations (12.1) are, finally, used to derive an infinite system of ordinary differential equations for the three-times-infinite expansion coefficients, which are only functions of the time. This elegant integration procedure is in principle applicable to any closed geometry and was applied by Rao to computationally determine the solutions for rectangular basins of constant depth. For details see [33, 39, 40] and the Appendix to this chapter.

12.7 A 'Second-Class' of Inertial Waves: 'Inertial Waves Proper'

In the preceding analysis, gravity waves on the rotating Earth were studied as plane waves in an infinite medium, as bounded waves in a semi-infinite space, in channels and enclosed basins. The construction of solutions to these waves was attributed to Sverdrup, Kelvin, Taylor, and Poincaré. Gravity was important in their description. It entered the equations for a homogeneous fluid via the deformation of the free surface, as the associated water column establishes via gravity the necessary pressure gradient that drives the oscillations. When applying the rigid lid assumption, this gravity-induced pressure is absent and these barotropic waves cannot exist.

The loss of existence of these waves when the fluid is confined to a rigid container is due to the assumption that the pressure is decomposed into the gravity dependent quasistatic external contribution plus a dynamic contribution induced by the internal motion, which is ignored. Another class of long Sverdrup, Kelvin and Poincaré waves should, therefore, also exist when the rigid lid assumption is imposed (the container is rigid and completely filled by the fluid of uniform density), but these internal dynamic pressure gradients are not ignored in the momentum equations. These waves are also long, but they are considerably shorter than the gravity waves, with wave lengths of the container dimensions (the depth) or shorter. In a homogeneous fluid in a basin of constant depth, these waves and oscillations have been thoroughly studied by Maas [21]. His work also gives an extensive literature review. These waves are also called 'inertial waves', because they are only driven by the rotation of the container, which, in the application here is vertical

to the confining container bottom and lid.[11] They have a frequency which may be different from the rotation frequency f. (Note that in Sect. 12.6.3 oscillations were called inertial when the circular frequency agreed with the inertial frequency.) This is the reason, why we use the attribute 'second class'. Maas occasionally uses the term 'inertial waves proper', which is probably more appropriate, since the attribute 'second class' is commonly an identifier for Rossby-type vorticity waves. He also states: 'Inertial waves proper are often neglected in thin-fluid systems as ocean and atmosphere because they have small wave lengths, and because of the stratification of these media. The scale length of inertial waves is the depth-scale of the vertical mode considered, which is therefore small, making the wave more susceptible to viscous degradation. Relative to this length scale, long waves thus appear only when their frequencies approach the inertial frequency f. However, for 'fat bodies' [20], like the Earth's core [and] stellar interiors [...] it is natural to consider these waves over a broader subinertial frequency range'. Suggestions on the oceanic relevance appeared in the literature, so that their occurrence in spectra of current meters and thermistor registrations for lake measurements is worth being scrutinized. Most probable is their observation in large and deep ice covered lakes such as Lake Vostok or Lake Baikal in winter.

Very briefly, solutions for the axial cylinder were found by Kelvin [13]. Bryan [3] gave the analysis of exact solutions in an axial spheroid to which Rieutord et al. [43] constructed the toroidal modes, lacking radial displacements. Maas analyzed infinite and semi-infinite channels of constant width and depth and rectangular boxes, all with the angular velocity parallel to the edges, see Fig. 12.21.

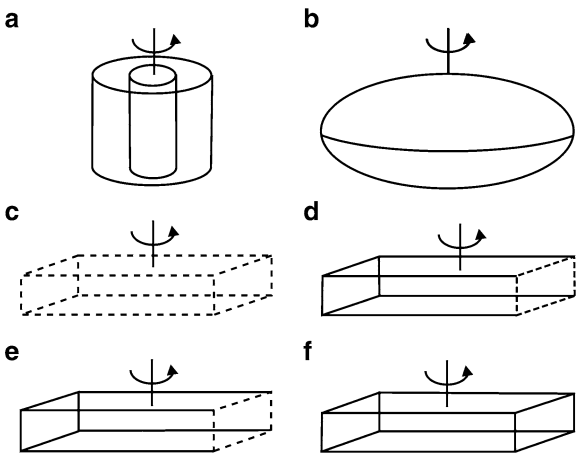

Fig. 12.21 Geometries for which 'inertial waves proper' have been constructed (**a**) axial cylindrical can or annulus, (**b**) axial spheroid, (**c**) infinite layer compressed between two parallel planes, (**d**) infinite channel, (**e**) semi-infinite duct, and (**f**) rectangular box. In all these cases, the rotation axis is a geometric symmetry axis. From [21]). © Fluid Dynamics Research, reproduced with permission

[11] For the geophysical application here the second Coriolis parameter $\tilde{f}$ is still ignored. So these inertial waves are long.

12.7.1 Governing Equations

Small amplitude waves in a homogeneous fluid that is rotating with angular frequency $\bar{\Omega}$ about a vertical axis aligned in the $\bar{z}$-direction (overbars denote dimensional quantities) are governed by the linearized, inviscid equations of motion on an $\bar{f}$-plane (where $\bar{f} = 2\bar{\Omega}$)

$$\begin{aligned}
&\frac{\partial \bar{u}}{\partial \bar{t}} - \bar{f}\bar{v} = -\frac{1}{\bar{\rho}}\frac{\partial \bar{p}}{\partial \bar{x}},\\
&\frac{\partial \bar{v}}{\partial \bar{t}} + \bar{f}\bar{u} = -\frac{1}{\bar{\rho}}\frac{\partial \bar{p}}{\partial \bar{y}},\\
&\frac{\partial \bar{w}}{\partial \bar{t}} = -\frac{1}{\bar{\rho}}\frac{\partial \bar{p}}{\partial \bar{t}},\\
&\frac{\partial \bar{u}}{\partial \bar{t}} + \frac{\partial \bar{v}}{\partial \bar{y}} + \frac{\partial \bar{w}}{\partial \bar{t}} = 0,
\end{aligned} \tag{12.57}$$

in which the usual notation has been used and $\bar{\rho} = \text{const.}$ (Note that in $(12.57)_3$ the hydrostatic assumption cannot be made since no gravity term is present.) In an infinite medium, the variables $(\bar{u}, \bar{v}, \bar{w})$ and $\bar{p}$ can be written as mono-chromatic waves, viz.,

$$(\bar{u}, \bar{v}, \bar{w}, \bar{p}) = (\bar{\tilde{u}}, \bar{\tilde{v}}, \bar{\tilde{w}}, \bar{\tilde{p}})\exp(-i\bar{\omega}\bar{t}), \tag{12.58}$$

leading to equations equivalent to (12.57) with $\partial(\cdot)/\partial\bar{t}$ replaced by $(-i\bar{\omega})$. If in these equations all velocity variables are eliminated, the so-called Poincaré equation [30, 31]

$$\frac{\partial^2 \bar{\tilde{p}}}{\partial \bar{x}^2} + \frac{\partial^2 \bar{\tilde{p}}}{\partial \bar{y}^2} - \left(\frac{\bar{f}^2}{\bar{\omega}^2} - 1\right)\frac{\partial^2 \bar{\tilde{p}}}{\partial \bar{z}^2} = 0 \tag{12.59}$$

for the pressure is obtained. For $\bar{\omega}^2 < \bar{f}^2$ this is a (hyperbolic) wave equation; for $\bar{\omega}^2 > \bar{f}^2$ it is elliptic instead. Plane waves are of the form

$$\bar{\tilde{p}}(\bar{x}, \bar{y}, \bar{z}) = \check{p}\,\exp(i\bar{\mathbf{k}}\cdot\bar{\boldsymbol{x}}), \tag{12.60}$$

where the wavenumber vector is $\bar{\mathbf{k}} \hat{=} (\bar{k}, \bar{\ell}, \bar{n})$. With (12.60), (12.59) implies the dispersion relation

$$\frac{\bar{\omega}}{\bar{f}} = \pm\frac{\bar{n}}{(\bar{k}^2 + \bar{l}^2 + \bar{n}^2)^{1/2}} = \pm\sin\phi, \tag{12.61}$$

where ϕ is the angle between $\bar{\mathbf{k}}$ and the plane perpendicular to the rotation axis. For $\bar{\omega}^2 < \bar{f}^2$, these waves are truly plane, not boundary trapped, with particle displacements which are largest in the interior of the fluid domain, resulting in a cellular wave pattern [1]. In the terminology of Platzman [29] and Mortimer [26],

they would be called Sverdrup-waves; however, they were already constructed by Poincaré [30] and are, therefore, called Poincaré waves by Maas [21].

For a layer with rigid bottom at $\bar{z} = -\bar{H}$ and rigid lid at $\bar{z} = 0$, it is readily seen that equations (12.57) enforce standing waves in the vertical with $\bar{w} = 0$ at $\bar{z} = (0, -\bar{H})$. Thus, we make the dynamically consistent ansatz

$$\begin{aligned} \bar{w} &= \sum_{n=1}^{\infty} \frac{\partial \bar{\zeta}_n}{\partial \bar{t}} \sin\left(\frac{n\pi\bar{z}}{\bar{H}}\right), \\ (\bar{u}, \bar{v}, \bar{p}) &= \sum_{n=1}^{\infty} (\bar{u}_n, \bar{v}_n, \bar{p}_n) \cos\left(\frac{n\pi\bar{z}}{\bar{H}}\right). \end{aligned} \tag{12.62}$$

Here, the subscript n refers to the n^{th} vertical mode. When substituting (12.62) into (12.57), it is straightforward to show that the amplitude functions satisfy the equations

$$\begin{aligned} \frac{\partial \bar{u}_n}{\partial \bar{t}} - \bar{f}\bar{v}_n &= -\bar{H}_n \frac{\partial^3 \bar{\zeta}_n}{\partial \bar{x} \partial \bar{t}^2}, \\ \frac{\partial \bar{v}_n}{\partial \bar{t}} + \bar{f}\bar{u}_n &= -\bar{H}_n \frac{\partial^3 \bar{\zeta}_n}{\partial \bar{y} \partial \bar{t}^2}, \\ \frac{\partial \bar{\zeta}_n}{\partial \bar{t}} + \bar{H}_n \left(\frac{\partial \bar{u}_n}{\partial \bar{x}} + \frac{\partial \bar{v}_n}{\partial \bar{y}}\right) &= 0, \end{aligned} \tag{12.63}$$

where

$$\bar{H}_n := \frac{\bar{H}}{n\pi}, \quad \bar{p}_n := \bar{\rho}\bar{H}_n \frac{\partial^2 \bar{\zeta}_n}{\partial \bar{t}^2}. \tag{12.64}$$

Formally, these equations agree with (12.1) except that the wave acceleration $\bar{H}_n \partial^2(\zeta_n)/\partial \bar{t}^2$ replaces the acceleration $\bar{g}$.

We now scale (12.63) and (12.64) by introducing the following dimensionless variables:

$$(x, y) = \frac{1}{\bar{H}_n}(\bar{x}, \bar{y}), \quad (u, v, \zeta) = \frac{1}{\bar{H}_n}(\bar{u}_n, \bar{v}_n, \bar{\zeta}_n), \quad (t, \omega^{-1}) = \bar{f}(\bar{t}, \bar{\omega}^{-1}). \tag{12.65}$$

With these relations (12.63) take the forms

$$\begin{aligned} \frac{\partial u}{\partial t} - v + \frac{\partial^3 \zeta}{\partial t^2 \partial x} &= 0, \\ \frac{\partial v}{\partial t} + u + \frac{\partial \zeta}{\partial t^2 \partial y} &= 0, \\ \frac{\partial \zeta}{\partial t} + \frac{\partial u}{\partial x} + \frac{\partial v}{\partial y} &= 0. \end{aligned} \tag{12.66}$$

Differentiation of $(12.66)_{1,2}$ with respect to t and elimination of u and v, respectively, yields the polarization equations, relating the velocity and elevation fields via

$$\begin{aligned} \mathcal{L}u &= \frac{\partial^2}{\partial t^2}\left(\frac{\partial^2 \zeta}{\partial t \partial x} + \frac{\partial \zeta}{\partial y}\right), \\ \mathcal{L}v &= \frac{\partial^2}{\partial t^2}\left(\frac{\partial^2 \zeta}{\partial t \partial y} - \frac{\partial \zeta}{\partial x}\right), \end{aligned} \tag{12.67}$$

where

$$\mathcal{L} := -\left(\frac{\partial^2}{\partial t^2} + 1\right). \tag{12.68}$$

These equations, when combined with $(12.66)_3$, imply the single differential equation

$$\left[1 + \left(1 - \nabla_H^2\right)\frac{\partial^2}{\partial t^2}\right]\frac{\partial \zeta}{\partial t} = 0 \tag{12.69}$$

for the vertical displacement field, where ∇_H^2 is the horizontal Laplace operator. With

$$(u, v, \zeta) = (\breve{u}, \breve{v}, \breve{\zeta})\exp(-\mathrm{i}\omega t), \tag{12.70}$$

Equation (12.69) implies that $\breve{\zeta}$ satisfies the Helmholtz equation

$$(\nabla_H^2 + \kappa^2)\breve{\zeta} = 0, \qquad \kappa^2 := \frac{1 - \omega^2}{\omega^2}, \tag{12.71}$$

where $\omega \langle 1$ for $\kappa^2 \rangle 0$. Moreover, with (12.66) and representations (12.70) the spatial part of the horizontal velocities is given by

$$\breve{u} = \frac{1}{\kappa^2}\left(-\mathrm{i}\omega\frac{\partial \breve{\zeta}}{\partial x} + \frac{\partial \breve{\zeta}}{\partial y}\right), \quad \breve{v} = \frac{1}{\kappa^2}\left(-\mathrm{i}\omega\frac{\partial \breve{\zeta}}{\partial y} - \frac{\partial \breve{\zeta}}{\partial x}\right). \tag{12.72}$$

It is noteworthy that these waves exist as plane waves in $\mathbb{R}^2$, when they have subinertial frequencies $\omega^2 < 1$ ($\bar{\omega}^2 < \bar{f}^2$). For $\omega^2 > 1$, they are exponentially amplified or evanescent and thus can only exist in bounded regions. We shall now briefly discuss the various cases.

12.7.2 Plane Inertial Sverdrup (Poincaré) Waves

A vertically standing mode of the form (12.62) may propagate horizontally as a plane wave of the form

$$(u, v, \zeta) = (\hat{u}, \hat{v}, \hat{\zeta})\exp[\mathrm{i}(kx + \ell y - \omega t)] \tag{12.73}$$

with

$$(\breve{u}, \breve{v}, \breve{\zeta}) = (\hat{u}, \hat{v}, \hat{\zeta}) \exp[\mathrm{i}(kx + \ell y)]. \tag{12.74}$$

Owing to $(12.71)_2$ these waves satisfy the dispersion relation

$$\kappa^2 = \frac{1-\omega^2}{\omega^2} = k^2 + l^2 \quad \rightarrow \quad \omega = \frac{1}{\sqrt{1+k^2+\ell^2}} = \frac{1}{\sqrt{1+\kappa^2}}. \tag{12.75}$$

This leads to the following expressions for the phase and group speeds, c_{ph} and c_{gr}, respectively:

$$c_{\mathrm{ph}} = \frac{\omega}{\kappa} = \frac{1}{\kappa\sqrt{1+\kappa^2}}, \qquad c_{\mathrm{gr}} = \frac{\mathrm{d}\omega}{\mathrm{d}\kappa} = -\frac{\kappa}{(1+\kappa^2)^{3/2}}, \tag{12.76}$$

which shows that phase and group move in opposite directions parallel and anti-parallel to the wave vector $\mathbf{k} \mathrel{\hat{=}} (k, \ell)$. Figure 12.22 displays graphs of the dispersion relation and the two speeds.

12.7.3 Inertial Kelvin Waves

By definition, Kelvin waves are rotation influenced motions for which the velocity component in one horizontal spatial direction vanishes. To see whether (12.66) permits such solutions, we assume $v(x, y, t) \equiv 0$ but $u(x, y, t) \neq 0$. Then, (12.66) takes the forms

$$\frac{\partial u}{\partial t} + \frac{\partial^3 \zeta}{\partial t^2 \partial x} = 0, \quad u + \frac{\partial^3 \zeta}{\partial t^2 \partial y} = 0, \quad \frac{\partial \zeta}{\partial t} + \frac{\partial u}{\partial x} = 0. \tag{12.77}$$

From $(12.77)_{1,3}$ there follows

$$\frac{\partial}{\partial t}(u - u_{xx}) = 0. \tag{12.78}$$

This shows that along-wall velocities u either grow or decay as $\exp(\pm x)$ with along wall distance. The general solution of (12.77) with $v \equiv 0$ is seen to be

$$(u, v, \zeta) = (\breve{u}, 0, \breve{\zeta}) \exp[-x + \mathrm{i}(ky - \omega t)] \tag{12.79}$$

with

$$\breve{\zeta} = \frac{\mathrm{i}}{\omega}\breve{u}, \tag{12.80}$$

the dispersion relation

$$\omega = -\frac{1}{k} \tag{12.81}$$

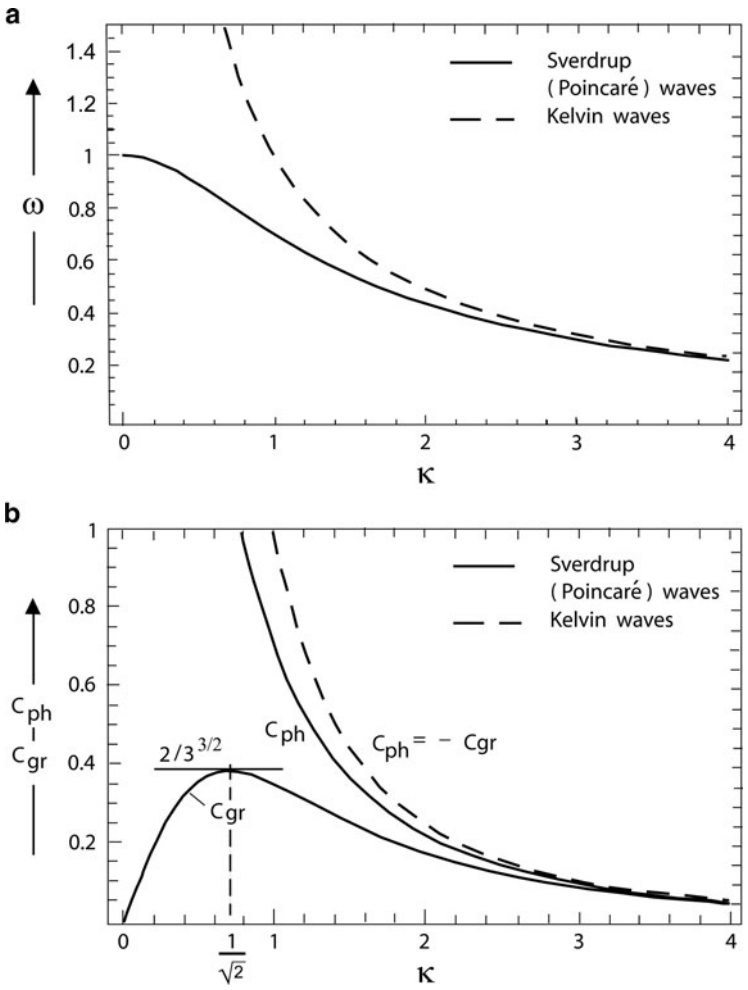

Fig. 12.22 (**a**) Dispersion relation for inertial Sverdrup (Poincaré) (*solid*) and inertial Kelvin (*dashed*) waves giving frequency ω vs. wavenumber amplitude κ. (**b**) Corresponding phase velocity (c_{ph}) and group velocity (c_{gr}) as functions of κ. For inertial Kelvin waves $c_{\mathrm{ph}} = -c_{\mathrm{gr}}$ (adapted from [21]). © Fluid Dynamics Research, reproduced with permission

and the phase, c_{ph}, and group, c_{gr}, velocities given by $c_{\mathrm{ph}} = -1/k^2$ and $c_{\mathrm{gr}} = 1/k^2$, respectively, see Fig. 12.22. Hence, energy propagates in a direction opposite to the phase. Inertial Kelvin waves thus decay in the direction of increasing x, while propagating their phase in the direction of decreasing y (more generally: the phase propagates to the right of decreasing wave amplitude (on the Northern hemisphere)). With reference to Fig. 12.23 this wave is trapped to the boundary at $x = 0$, and its energy propagates in the positive y-direction. However, since there are no lines parallel to the x-axis at which the u-velocity component would vanish, these Kelvin

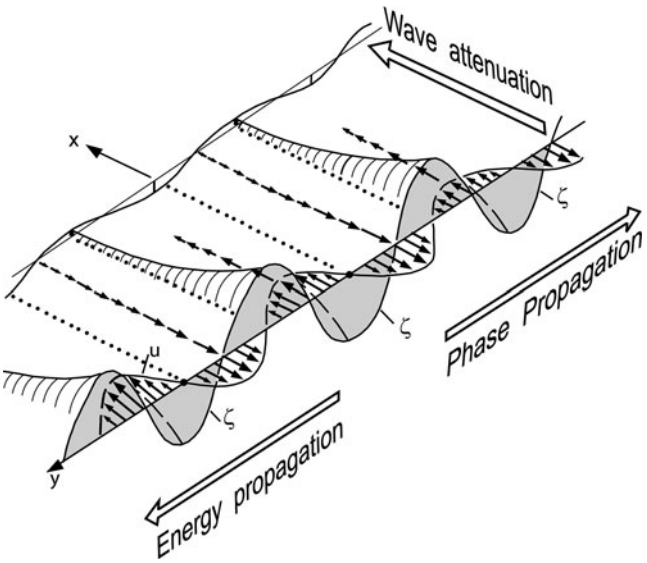

Fig. 12.23 In an inertial Kelvin wave with horizontal velocities in the x-direction, this velocity and the vertical displacements decay in the positive x-direction, whilst the phase propagates in the negative and the energy in the positive y-direction. The variables u and ζ are out of phase by $\pi/2$

waves do not exist in infinite space per se. They play, however, an essential role when Poincaré waves are reflected at a channel end.

12.7.4 Inertial Poincaré Waves in a Channel

If we assume the existence of a wall at $x = 0$ with no through-flux, then $u = 0$ at $x = 0$, implying from $(12.67)_1$

$$\frac{\partial^2 \zeta}{\partial t \partial x} + \frac{\partial \zeta}{\partial y} = 0 \qquad \text{at} \qquad x = 0. \tag{12.82}$$

A pair of incoming and reflected waves with identical frequency ω and along-wall wavenumber ℓ is given by

$$\zeta = Z_i \exp\left[\mathrm{i}(-kx + \ell y - \omega t + \phi)\right] + Z_r \exp\left[\mathrm{i}(kx + \ell y - \omega t - \phi)\right] \tag{12.83}$$

and needs to satisfy $(12.82)_1$ or

$$-\omega \frac{\partial \zeta}{\partial x} + \ell \zeta = 0 \qquad \text{at} \qquad x = 0, \tag{12.84}$$

implying, in view of (12.83),

$$Z_i(\mathrm{i}k\omega + \ell)\exp(\mathrm{i}\phi) + Z_r(-\mathrm{i}k\omega + \ell)\exp(-\mathrm{i}\phi) = 0.$$

This can also be written as

$$\frac{Z_i}{Z_r} = \frac{(k\omega + \mathrm{i}\ell)}{(k\omega - \mathrm{i}\ell)}\frac{\exp(-\mathrm{i}\phi)}{\exp(\mathrm{i}\phi)}. \tag{12.85}$$

In this expression, the denominator is the complex conjugate of the numerator, say, $r\exp(i\theta)/\,r\exp(-i\theta) = \exp(2i\theta)$ for some amplitude r and angle θ. This also shows that the reflected wave has the same amplitude as the incoming wave, so we may set $Z_i = Z_r = Z/2$. The two waves only suffer a phase shift. With $Z_i/Z_r = 1$, (12.85) implies

$$\exp(-2\mathrm{i}\phi) = \frac{k\omega - \mathrm{i}\ell}{k\omega + \mathrm{i}\ell} \quad \Rightarrow \quad \tan\phi = \frac{\ell}{k\omega}. \tag{12.86}$$

Moreover, perpendicular to the wall the resulting wave is standing; we may thus rewrite (12.83) as

$$\begin{aligned}\zeta &= Z\cos(kx - \phi)\exp[\mathrm{i}(\ell y - \omega t)]\\ &= Z\{\cos(kx)\cos\phi + \sin(kx)\sin\phi\}\exp[\mathrm{i}(\ell y - \omega t)]\\ &= \underbrace{Z\cos\phi}_{\mathcal{Z}}\{\cos(kx) + \frac{\ell}{k\omega}\sin kx\}\exp[\mathrm{i}(\ell y - \omega t)]\end{aligned} \tag{12.87}$$

with the newly defined amplitude $\mathcal{Z} = Z\cos\phi$. With the form (12.87) of the vertical displacement function, $(12.72)_1$ can be used to compute the cross-wall and along-channel velocity components. This straightforward computation yields for the *cross-wall velocity component*

$$u = \mathrm{i}k\mathcal{Z}\frac{\omega^3}{1-\omega^2}\left(1 + \left(\frac{\ell}{\omega k}\right)^2\right)\sin kx\ \exp[\mathrm{i}(\ell y - \omega t)] \tag{12.88}$$

and for the *along-channel velocity component*

$$v = \mathcal{Z}\left(-\ell\omega\cos kx + \frac{1}{k}\sin kx\right)\exp[\mathrm{i}(\ell y - \omega t)]. \tag{12.89}$$

It is evident from (12.88) that the cross-wall wavenumber k can be quantized when a second wall is erected at $x = L$. Then

$$k \in \left\{k_m = \frac{m\pi}{L}, \quad m = 1, 2, 3, \ldots\right\}. \tag{12.90}$$

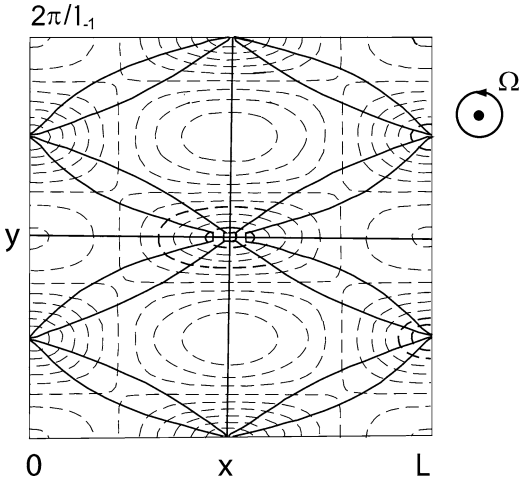

Fig. 12.24 Top view of one wave length segment of a channel which is infinitely long in the y-direction and of dimensionless width $L = 4$ in x-direction. It shows phase (*solid*) and amplitude (*dashed*) lines of the vertical displacement field of a pair of equal amplitude, mode-1, up and down channel propagating Poincaré modes of frequency $\omega = 0.7$. Amplitudes are maximal at the saddle nodes of phase lines, located on the channel axis, at $1/4$ and $3/4$ wave length. The rotation axis, designated Ω, points out of the paper (redrawn from [21]). © Fluid Dynamics Research, reproduced with permission

So, inertial Poincaré waves exist in infinitely long channels as isolated countable infinite modes.

The up- and down-channel solutions (12.87)–(12.90) of inertial Poincaré waves develop amphidromic structures similar to gravity driven Poincaré waves. Figure 12.24 shows this amphidromic system for such a mode-1 quasi-standing wave as constructed by Maas [21]. The mode structure is characterized by phase lines circling anti-cyclonically (i.e. clockwise) around nodal points where vertical elevation vanishes. According to Maas 'such phase pattern was first suggested long ago by Whewell [47] to comprehensively describe observed tidal elevation patterns, see [4]'.

12.7.5 Inertial Poincaré Channel Waves Reflecting from a Vertical Wall

Recall that classical gravity (externally) driven Kelvin waves can be combined by equal-amplitude forward and backward moving propagating Kelvin waves with the same frequency to form quasi-standing Kelvin waves in an infinite channel. Per se, these could not form a solution in a channel bounded from one side, because the no-flux condition through such an (imaginary) wall could not be satisfied. To achieve

such a no-flux condition through the end-wall, an infinite number of backward moving (reflected) Poincaré waves with the same frequency had to be added and adequately combined. This was Taylor's solution [45].

Such a solution cannot be found with inertial Kelvin waves. However, an inertial Poincaré wave entering a channel can be combined with a trapped inertial Kelvin wave and an infinite number of backward moving inertial Poincaré channel waves. Let us assume that the wave propagates in the y-direction and the across-channel wavenumber is $k_m = m\pi/L$. Then, the along-channel wavenumber ℓ_m can be deduced from $(12.71)_2$ to yield

$$\ell_m = \pm\left(\frac{1}{\omega^2} - (1 + k_m^2)\right)^{1/2} = \pm\left(\frac{1}{\omega^2} - \frac{1}{\omega_m^2}\right)^{1/2}, \tag{12.91}$$

where

$$\omega_m := (1 + k_m^2)^{-1/2} < 1 \tag{12.92}$$

is the cut-off frequency. For $|\ \omega\ | < |\ \omega_m\ |$, ℓ_m is real and inertial Poincaré waves exist as propagating waves; for $|\ \omega\ | > |\ \omega_m\ |$, they are exponentially evanescent or growing.

Consider a reflection at $y = 0$ for a mode-1 ($m = 1$) Poincaré wave approaching the wall at $y = 0$ from positions with $y > 0$. The total along channel velocity is thus composed of an incoming Poincaré wave (of given amplitude, here chosen to be unity, (12.89), $\mathcal{Z} = 1$) and having along channel wavenumber $+\ell_1$,

$$v^{\text{in}}_{\text{Poincaré}}(x, y, t) = \{-\ell_1\omega\cos k_1 x + \frac{1}{k_1}\sin k_1 x\} \times \exp(\mathrm{i}\ell_1 y), \tag{12.93}$$

plus a trapped inertial Kelvin wave ((12.79), but in the y-direction)

$$v^{\text{trapped}}_{\text{Kelvin}}(x, y, t) = v_0 \exp\left(-y + \frac{\mathrm{i}}{\omega}x\right), \tag{12.94}$$

plus an infinite sum of reflected inertial Poincaré waves, again of the form (12.89), but with a negative sign of the along-channel wavenumber

$$v^{\text{out}}_{\text{Poincaré}}(x, y, t) = \sum_{m=1}^{\infty} v_m\{\ell_m\omega\cos k_m x + \frac{1}{k_m}\sin k_m x\} \times \exp(-\mathrm{i}\ell_m y). \tag{12.95}$$

In (12.93)–(12.95), a common exponential factor $\exp(-i\omega t)$ has been dropped. The unknown complex valued amplitudes $v_0, v_1, v_2, \ldots$ follow from the no-flux condition at $y = 0$

$$\begin{aligned} &v^{\text{in}}_{\text{Poincaré}}(x, 0) + v^{\text{trapped}}_{\text{Kelvin}}(x, 0) + v^{\text{out}}_{\text{Poincaré}}(x, 0) \\ &\quad = \left[\left(-\ell_1\omega\cos k_1 x + \frac{1}{k_1}\sin k_1 x\right)\exp(\mathrm{i}\ell_1 y) + v_0\exp\left(-y + \frac{\mathrm{i}x}{\omega}\right)\right. \end{aligned}$$

$$+\sum_{m=1}^{\infty} v_m \left\{ \ell_m \omega \cos k_m x + \frac{1}{k_m} \sin k_m x \right\} \exp(-\mathrm{i}\ell_m y) \Big]_{y=0}$$
$$= -\ell_1 \omega \cos k_1 x + \frac{1}{k_1} \sin k_1 x + v_0 \exp\left(\frac{\mathrm{i}x}{\omega}\right)$$
$$+\sum_{m=1}^{\infty} v_m \left\{ \ell_m \omega \cos k_m x + \frac{1}{k_m} \sin k_m x \right\} = 0. \tag{12.96}$$

Note that the inertial Poincaré waves with mode numbers $m > 1$ are all trapped (exponentially evanescent for $y > 0$). So, we define

$$\ell_m = -\mathrm{i}\left(\frac{1}{\omega_m^2} - \frac{1}{\omega^2}\right)^{1/2} = -\mathrm{i}s_m \quad (s_m > 1). \tag{12.97}$$

Equation (12.96) has been solved by Maas [21] using the collocation method. In this method, the infinite sum is truncated at $M - 1$. Writing (12.96) then for M different values of $x \in [0, L]$ yields a linear system of equations for the amplitudes $v_0, v_1, v_2, \ldots, v_{(M-1)}$. Figure 12.25 is based on a solution constructed with $M = 21$. It shows in panel (a) the amplitude (dashed) and phase (solid) of the vertical displacement field ζ. The phase propagates in the clockwise direction, whilst the energy does so in the anti-clockwise direction. Panel (b) in Fig. 12.25 shows corresponding horizontal velocity ellipses at a number of positions. These are traversed in the clockwise direction, and are very thin and along the channel sides at the boundaries, so that the velocity component perpendicular to the boundary vanishes.

12.7.6 Inertial Waves in Rectangular Basin of Constant Depth

Inertial waves also exist in fully enclosed basins as has been demonstrated by Maas [21] for rectangles by using the spectral method of Proudman [33] and Rao [40] (see Appendix to this chapter). This solution method uses a Helmholtz decomposition of the velocity field $\mathbf{v} = \mathbf{v}^{\phi} + \mathbf{v}^{\psi}$ with $\mathbf{v}^{\phi} = -\nabla\phi$, $\mathbf{v}^{\psi} = \hat{\mathbf{k}} \times \nabla\psi$, where $\hat{\mathbf{k}}$ is a unit vector aligned with the rotation axis. The no-flux condition at the boundary with unit normal vector $\mathbf{n}$ is then transformed to the statements

$$(\mathrm{grad}\,\phi) \cdot \mathbf{n} = 0, \qquad \psi = 0 \qquad \text{along} \quad \partial\mathcal{D}. \tag{12.98}$$

The velocity potential ϕ, the stream function ψ and the elevation field ζ are then represented as

$$(\phi, \psi, \zeta) = \sum_{\alpha} (p_\alpha \phi_\alpha,\ q_\alpha \psi_\alpha,\ r_\alpha \zeta_\alpha) \tag{12.99}$$

in terms of complete function sets $\{\phi_\alpha\}$, $\{\psi_\alpha\}$ (with $\zeta_\alpha \propto \phi_\alpha$), where α is a binary index ($\alpha = (k, \ell)$ for the (k, ℓ)-mode). These functions follow from suitably

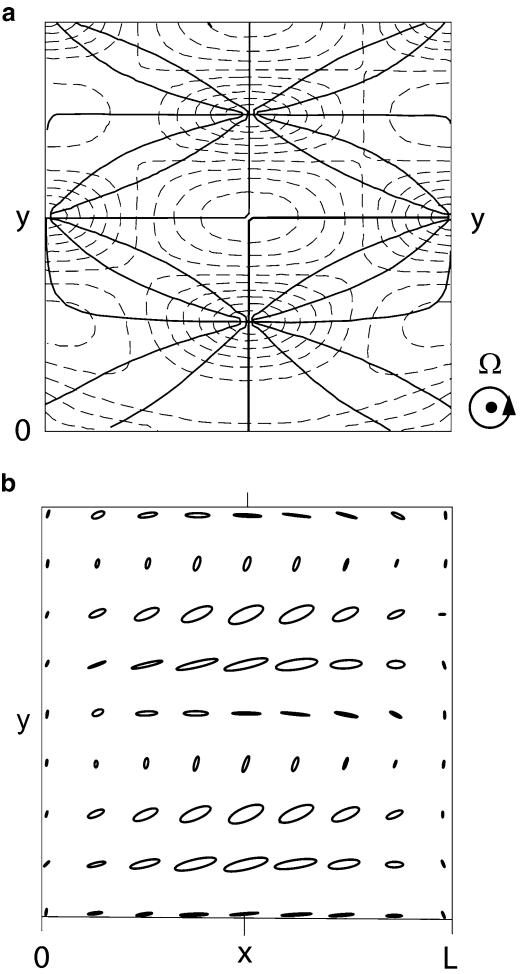

Fig. 12.25 Top view of (**a**) phase (*solid*) and amplitude (*dashed*) of the vertical displacement field of a mode-1, down-channel propagating inertial Poincaré mode of frequency $\omega = 0.7$ in a channel of dimensionless width $L = 4$, reflecting from a vertical wall at $y = 0$. During reflection inertial Kelvin and inertial Poincaré waves are excited, that are trapped in the y-direction. Phase lines are given every 30° which rotate anti-cyclonically around the amphidromes at the central axis (the rotation axis, Ω, is out of the paper; (**b**) horizontal current ellipses once traversed clockwise for $\omega > 0$ during one period (redrawn from [21]). © Fluid Dynamics Research, reproduced with permission

chosen selfadjoint elliptic eigenvalue problems, adjusted to the geometry of the fluid domain but not related to the dynamical equations except the flux condition through the boundary. The coefficients $p_\alpha, q_\alpha, r_\alpha$ are functions of time only. By substituting the representations (12.99) into the dynamical equations (here (12.106) and (12.107) in the Appendix) then yields a system of ordinary differential equations

for them. Some details of this method are presented in the Appendix to this chapter. This method of integration seems to be economical only for simple geometries. Proudman [33] suggested it and used it for the axial cylinder of uniform and parabolic depth shape, Rao [40] used the method to retrieve and extend Taylor's [45] results for rotational gravity waves in rectangles, and Maas [21] applied it to oscillations of 'inertial waves proper' in the rectangle. For the difficult particulars of the application of the method to rectangles we refer to Rao [40] and Maas [21].

In what follows, we shall only present the elevation and velocity fields of the first three modes in a rectangle of dimensionless size $2\pi \times \pi$. Maas needed 91 Fourier modes ($\alpha = 1, 2, 3, \ldots, 91$) to obtain five digits accuracy in the elevation and velocity fields. He writes [21]:

"When a vertical mode is picked, say $n = 1$, and the basin is scaled with the corresponding vertical scale, the eigenfrequencies are determined, and the corresponding elevation amplitude and velocity fields can be plotted. (Note that the actual vertical elevation is depth dependent, due to the vertical mode dependence, as in $(12.62)_1$.) Counting from the top-down, the first three modes are shown in Fig. 12.26 in a rectangular horizontal cross-section of the $2\pi \times \pi$ rectangular parallelepiped. Modes 1 and 3 have antisymmetric elevation (left) and symmetric velocity fields (right), and vice versa for mode 2. The pictures present the following information. In the elevation field ζ (at the left), colouring and dashed lines represent elevation amplitudes. Deep blue corresponds with zero elevation, red with maximum amplitudes. Phase lines (every 30°) are solid. They end in nodal (zero elevation) points and show that phase is circling around the amphidromes in either clockwise or anti-clockwise direction. All amphidromes on the middle axis ($y = \pi/2$) are traversed in a clockwise sense, all others (close to $y = 0$ and π) in anti-clockwise sense. Orthogonal crossings of phase lines (as, e.g. in the centre of the rectangle for mode 2) imply equal phases on all four branches, implying that the whole real central region of mode 2 rises and sinks in unison. Anti-symmetry of the elevation field of, e.g. mode-1 is evident from a 180° phase change between mirror images about the centre point.

The velocity field (u, v) (at the right side of Fig. 12.26) contains, in principle, four independent parameters. Each component has an amplitude and a phase. At each individual location these can be represented in terms of a velocity ellipse, as e.g. in [45], expressed in terms of four other parameters: maximum amplitude, $u_{\max}$, ellipticity $u_{\min}/u_{\max}$, orientation of the main axis, Ψ and phase (with respect to this local orientation Φ) [32]. The ellipticity varies between -1 (circular clockwise, deep blue) and $+1$ (circular anti-clockwise, red), whilst it represents rectilinear motion when it is zero (green). The green colour at the boundary tells that the velocity is rectilinear there. Separate consideration of the inclination shows the velocity vector to be everywhere parallel to the sides. Maximum velocity $u_{\max}$ is represented by dashed lines".

Further discussions, including results concerning the frequency properties and the first four modes of a $(\pi \times \pi)$-square are given by Maas [21].

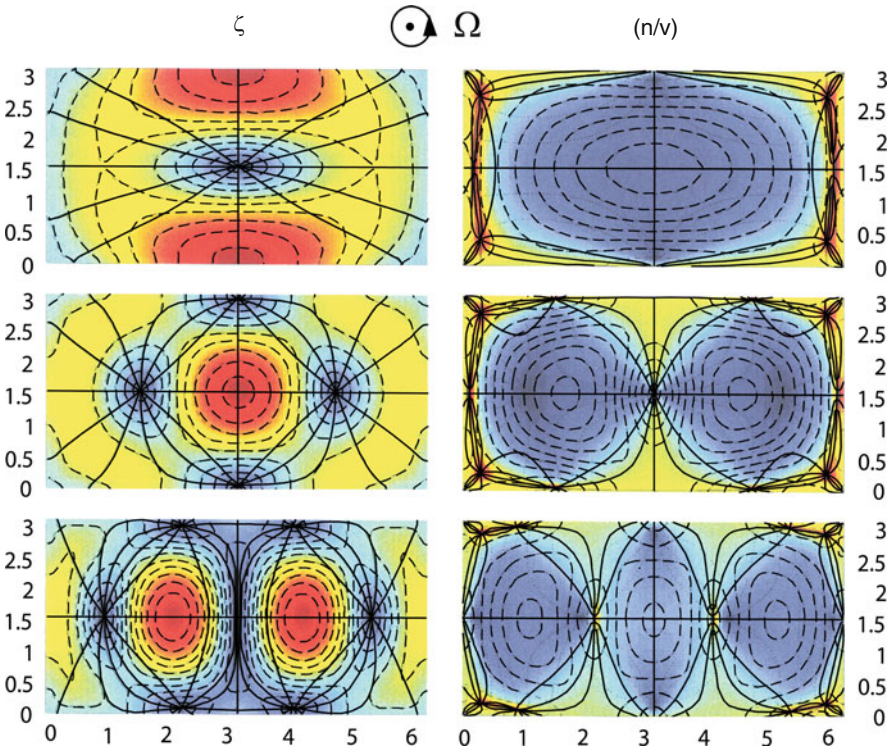

Fig. 12.26 Top view of elevation (*left*) and horizontal velocity (*right*) fields of a $2\pi \times \pi$ rectangle for mode 1, $\omega \approx 0.657$ (*top*); mode 2, $\omega \approx 0.564$ (*middle*); and mode 3, $\omega \approx 0.477$ (*bottom*). The rotation vector points out of the paper towards the reader; the tank thus moves anti-clockwise. For further explanation, see main text. Redrawn from [21]. © Fluid Dynamics Research, reproduced with permission

12.7.7 Discussion

In this section, inertial waves – better called 'inertial waves proper' or 'second class inertial waves' – were discussed, which are not supported by gravity but, apart from Coriolis effects, by dynamical pressure. Equations which are rather similar to the long wave equations, are obtained for each of the vertical modes that exist in a fluid layer having top and bottom perpendicular to the rotation axis. Acceleration due to gravity is replaced here by vertical acceleration in the wave field. The resulting horizontal problem was solved in the unbounded domain, in the infinite and semi-infinite channel and in rectangular basins.

Waves in the infinite plane are sub-inertial and known as inertial Sverdrup (or, according to a different nomenclature, Poincaré) waves. With one vertical boundary, along a straight line in the (x, y)-plane two plane waves can be combined into an inertial Poincaré wave whose velocity component normal to this wall vanishes.

This velocity component then vanishes also at an infinite number of other positions parallel to this wall, so that an additional wall can be placed at such a position, thus forming a channel. Inertial Kelvin waves have also been found as solutions having vanishing velocity component in one spatial direction. These waves then propagate the phase (energy) in a direction which is 90° to the right (to the left on the Southern hemisphere) of the direction of non-zero horizontal velocity (see Fig. 12.23), and this velocity as well as the corresponding particle motion decay exponentially with the velocity, making it incompatible with the existence of a solid boundary. So, free inertial Kelvin-waves proper do not exist.

The reflection of a channel inertial Poincaré wave from the end wall requires mathematically the addition of a trapped inertial Kelvin wave proper and an infinite number of reflected inertial Poincaré waves proper to achieve zero flux of fluid through the end wall. This implies that the inertial wave system in an enclosed rectangle consists of an additive combination of an infinite set of channel inertial Poincaré waves proper together with two inertial Kelvin waves proper, but we have expressed it as a combination of two intertwined infinite sets of spatial Fourier modes.

Maas [21], in his closing statements, mentions that 'the existence of (linear) wave solutions does not guarantee their stability'. He quotes for the axial can a proof of instability of inertial waves to short wavelength perturbations of oblique orientation [19] and muses that such instability results may extend also to rectangles.

The presentation of these waves in this book has been given, because under unusual circumstances it may not be unlikely that inertial waves proper may be observable in the field. This is likely the case in fully ice covered lakes under homogeneous conditions, when gravity driven motions in the water beneath the ice are considerably damped out, or non-existent at all. In those circumstances, also turbulent pulsations are effectively damped out. So, if inertial waves proper are excited, then they should be best observable in ice covered lakes. Of course, with wind forces being essentially absent, earthquakes then are the only remaining substantial triggering mechanisms of these waves. These give rise to a temporal Dirac-type displacement field of the solid boundary, which dies quickly out to zero. The induced motion in the aftermath of the earthquake within the lake region may then establish a resonant response of basin scale inertial waves proper.

Moreover, according to Maas [21], 'there seems to be no intrinsic reason to neglect these waves completely, despite their small-scale (order of the water depth) and to enforce solutions by the hydrostatic approximation. Krauss [15] observes that the hydrostatic approximation has been made ever since Laplace, but that a real motivation (except for the tautological statement that it applies to waves that are long compared with the water depth) is absent. Indeed, for this reason the approximation has been criticized by Solberg [44] when looking into these inertial 'cellular' waves, [...]. The failure of Laplace's Tidal Equations to even adequately model long surface waves in the presence of topographic variations was addressed by Chapman [5] and Chapman and Hendershott [6]'.

12.8 Concluding Discussion

In this chapter, the analysis of linear waves in a Boussinesq fluid on a permanently rotating frame was continued by studying such waves in semi-bounded and bounded basins of constant depth. By excluding depth variations, Rossby waves on the f-plane are automatically excluded. The goal of the chapter was twofold: (1) to construct gravity wave solutions of the linearized shallow water equations when the rotation of the Earth is included and (2) to present solutions for 'inertial waves proper' for barotropic fluids in domains with rigid boundaries. Concerning (1), this led to propagating and quasi-standing Kelvin and Poincaré waves in channels of constant width and constant depth. The impossibility of the existence of pure Kelvin and Poincaré waves in a semi-infinite gulf of a long rectangular basin led to Taylor's reflection problem, which showed that a pair of quasi-standing Kelvin waves had to be complemented by an infinite number of Poincaré waves with the same frequency and wavelengths of an integer fraction of the channel width in order to match the zero velocity condition across the channel width. If all the amplitudes of these infinite Poincaré waves are exponentially evanescent in the distance variable along the channel axis, then far from the gulf wall only the standing Kelvin wave survives and the reflection is called *complete*. Else, the quasi-standing Kelvin wave at large distances from the gulf wall is hidden in the 'noise' of the non-evanescent Poincaré waves; in this case, the reflection is called *incomplete*. Figure 12.13 shows in its eight panels a transition from complete to noisy incomplete reflection.

A quasi-standing oscillation of gravity waves in a rectangular basin of constant depth can be constructed by a superposition of a pair of standing Kelvin waves with two infinite numbers of propagating Poincaré waves with the same frequency, which move away from the respective walls. Identifying complete and incomplete reflection is only possible in oblong rectangles, because close to the bounding walls of the rectangle Kelvin and Poincaré activities are comparable.

It has, therefore, been desirable to employ a different solution technique for the seiche motion in (compact) rectangular basins of constant depth. This problem has a long history, starting with Lord Rayleigh at the beginning of the twentieth century and culminating with Rao's Ph.D dissertation in 1965. A historical account based on his work has been given in Sect. 12.6.1. The crucial idea, which allowed evaluation of the frequency relation with the least approximations (among the many) was the solution procedure proposed by Proudman in 1916, which is illustrated in the Appendix to this chapter. In essence, by using Helmholtz's theorem of additively decomposing a vector function into an irrotational and a solenoidal part, selfadjoint eigenvalue problems could be formulated, which Rao solved numerically by electronic computation. He also compared his frequency relation for a (1×1) and a (1×2) rectangle with experiments and demonstrated excellent agreement with the corresponding results obtained with a (1×1) and a (1×2) rectangle filled with a homogeneous fluid placed on a rotating table. His figures on the structure of amphidromies for various modes at varied rotation speeds demonstrate the complexities which seiches in a simple rectangle can take, certainly hardly predictable without a computational analysis.

The above analysis was conducted for linear gravity waves, i.e. waves which only exist when gravity is operating. In the mathematical approximation dealt with in this case, the pressure is purely hydrostatic. This means, in a homogeneous water mass, in which none of the surfaces bounding the water mass move (rigid lid), and no wind shear applies, the hydrostatic pressure drops out of the governing equations; the emerging gravity-free shallow water equations have only the zero solution. This is too restrictive; indeed, non-vanishing solutions of the shallow water equations can be reconstructed by adding the dynamical pressure gradients, see (12.57). Wave solutions of these equations are of another class and have been coined 'inertial waves proper'. They may be excited, e.g. in ice covered large lakes. Such waves have so far only been analyzed for simple geometries (see Fig. 12.21). Our presentation follows Maas [21], who constructed solutions for infinite channels and a homogeneous fluid in a rectangular box.

Plane inertial Sverdrup, inertial Kelvin and Poincaré waves do exist but exhibit physical behaviour which differs considerably from that of the corresponding gravity waves. Phase and group speeds of inertial Sverdrup and Kelvin waves propagate in different directions, see Fig. 12.23. Inertial quasi-standing Poincaré waves develop amphidromic systems similar to those of the classical standing Poincaré. Reflection of an inertial Kelvin wave at the end wall of a semi-infinite gulf does not exist; however, an incoming inertial Poincaré wave can be combined with a trapped Kelvin wave and an infinite number of outgoing Poincaré waves. So, inertial waves in rectangular basins of constant depth must also exist, and have indeed been constructed by Maas [21] using the Proudman–Rao decomposition technique explained in the Appendix to this chapter.

These wave types have not been applied to real ice covered lakes yet but indicate some promising potential of identification, say in Lake Baikal and Lake Vostok, etc.

12.9 Appendix: Solution Scheme of Proudman–Rao to Solve (12.1)

Proudman [33] suggested an elegant method to solve the equations describing the free linear oscillations of homogeneous water in an enclosed basin with variable depth and no inflow or outflow along the shore. It is assumed that the tidal motion takes place in a basin $\mathcal{D}$ completely enclosed by a rigid boundary, $\partial\mathcal{D}$, at which the no-through flow condition applies. The boundary value problem is given by (12.1) or

$$\begin{aligned} &\frac{\partial \zeta}{\partial t} + \nabla \cdot \mathbf{v} = 0, \\ &\frac{\partial \mathbf{v}}{\partial t} + f\hat{\mathbf{k}} \times \mathbf{v} = -g\nabla\zeta, \end{aligned} \qquad (x, y) \in \mathcal{D} \qquad (12.100)$$

subject to the boundary conditions

$$H\mathbf{v} \cdot \mathbf{N} = 0. \qquad (x, y) \in \partial\mathcal{D}. \qquad (12.101)$$

Here, all variables have their physical dimensions; furthermore, $\mathbf{v}, \zeta$ are functions of x, y, t; $\hat{\mathbf{k}}$ is a unit vector pointing in the $+z$-direction, g is the gravity constant, $H(x, y)$ the depth function and $\mathbf{N}$ is a unit vector in the (x, y)-plane perpendicular to the boundary $\partial\mathcal{D}$. It is further assumed that the region $\mathcal{D}$ is simply connected.

According to Helmholtz's theorem, the vector field $\mathbf{v}$ can be additively decomposed into two contributions, $\mathbf{v} = \mathbf{v}^{\phi} + \mathbf{v}^{\psi}$, such that

1. The kinetic energy is partitioned according to $K = K^{\Phi} + K^{\psi}$,

$$\underbrace{\frac{1}{2}\rho\int_{\mathcal{D}} \mathbf{v}\cdot\mathbf{v}HdA}_{K} = \underbrace{\frac{1}{2}\rho\int_{\mathcal{D}} \mathbf{v}^{\phi}\cdot\mathbf{v}^{\phi}HdA}_{K^{\phi}} + \underbrace{\frac{1}{2}\rho\int_{\mathcal{D}} \mathbf{v}^{\psi}\cdot\mathbf{v}^{\psi}HdA}_{K^{\psi}}, \tag{12.102}$$

   where dA is the increment of the surface area and ϕ, ψ have the meaning of a velocity potential and a stream function, respectively.
2. $\mathbf{v}^{\phi}$ and $\mathbf{v}^{\psi}$ are given by the relations

$$\mathbf{v}^{\phi} = -\nabla\phi, \qquad \mathbf{v}^{\psi} = h^{-1}\hat{\mathbf{k}}\times\nabla\psi, \tag{12.103}$$

   where $h = H/\bar{H}$ is the non-dimensional ratio of the actual depth $H(x, y)$ and the basin mean depth $\bar{H} = \frac{1}{A}\int_{\mathcal{D}} H(x, y)dA$.
3. At the boundary, the no-flux conditions imply the following Neumann and Dirichlet conditions

$$h\frac{\partial\phi}{\partial N} = h\nabla\phi\cdot\mathbf{N} = 0, \quad \psi = 0 \qquad (x, y)\in\partial\mathcal{D}, \tag{12.104}$$

   where $\partial(\cdot)/\partial N$ is the derivative normal to the boundary.
4. $\mathbf{v}^{\phi}$ and $\mathbf{v}^{\psi}$ are determined as functions of $\mathbf{v}$ by constructing from (12.103) the following inhomogeneous elliptic equations:

$$\begin{aligned}\nabla\cdot(h\nabla\phi) &= -\nabla\cdot(h\mathbf{v}^{\phi}) \stackrel{!}{=} -\nabla\cdot(h\mathbf{v}),\\ \nabla\cdot(h^{-1}\nabla\psi) &= -\nabla\cdot(\hat{\mathbf{k}}\times\mathbf{v}^{\psi}) \stackrel{!}{=} -\nabla\cdot(\hat{\mathbf{k}}\times\mathbf{v}).\end{aligned} \tag{12.105}$$

   (The expressions on the far right hold, since (12.103) implies $\nabla\cdot(h\mathbf{v}^{\psi}) \equiv 0$ and $\nabla\cdot(\hat{\mathbf{k}}\times\mathbf{v}^{\phi}) \equiv 0$, as can easily be proved).
5. Since $\mathbf{v}$ is unknown, the inhomogeneous equations (12.105) are not very helpful in that form. However, since $\mathbf{v}$ must satisfy (12.100) and (12.101), the procedure is to convert (12.105) into dynamical equations on ϕ and ψ, and, having determined ϕ and ψ in this way, to reconstruct $\mathbf{v}$ by means of (12.103). To this end, we represent ϕ and ψ in terms of the spectral functions of the following elliptic boundary value problems:

$$\left.\begin{aligned} -\nabla\cdot(h\nabla\phi_\alpha) &= \lambda_\alpha\phi_\alpha,\ (x,y)\in\mathcal{D},\\ h\frac{\partial\phi_\alpha}{\partial N} &= 0, \qquad\qquad (x,y)\in\partial\mathcal{D},\end{aligned}\right\} \tag{12.106}$$

$$\left.\begin{aligned} -\nabla\cdot(h^{-1}\nabla\psi_\alpha) &= \mu_\alpha\psi_\alpha,\ (x,y)\in\mathcal{D},\\ h^{-1}\psi_\alpha &= 0, \qquad\qquad (x,y)\in\partial\mathcal{D}\end{aligned}\right\} \tag{12.107}$$

Here, α is a counting index, $\alpha = 1,2,\ldots,\infty$, and $\lambda_\alpha, \mu_\alpha$ are eigenvalues of the Neumann problem (12.106) and the Dirichlet problem (12.107) respectively. Note that the eigenvalue problems (12.106) and (12.107) do not involve the time and are defined once the basin geometry is prescribed.

6. Along with the functions ϕ_α and ψ_α we may also define the functions

$$\mathbf{v}_\alpha^\phi := -\nabla\phi_\alpha, \qquad \mathbf{v}_\alpha^\psi := h^{-1}\hat{\mathbf{k}}\times\nabla\psi_\alpha, \tag{12.108}$$

provided the functions ϕ_α and ψ_α are uniquely defined by (12.106) and (12.107).

It is not difficult to show that the problems (12.106) and (12.107) are selfadjoint. Therefore, the eigenvalues are real, the spectra are discrete and the eigenfunctions internally[12] orthogonal and can be normalized; moreover, ϕ_α and ψ_α are square integrable. To prove orthogonality, we multiply $(12.106)_1$ with ϕ_β and integrate over $\mathcal{D}$. This yields

$$\begin{aligned} &-\int_{\mathcal{D}}[\nabla\cdot(h\nabla\phi_\alpha)]\phi_\beta\,dA\\ &\quad= -\int_{\mathcal{D}}\nabla\cdot(h\nabla\phi_\alpha\phi_\beta)dA + \int_{\mathcal{D}}h\nabla\phi_\alpha\cdot\nabla\phi_\beta\,dA\\ &\quad= -\int_{\partial\mathcal{D}}\phi_\beta\underbrace{h\nabla\phi_\alpha\cdot N}_{=0}\,d(A) + \int_{\mathcal{D}}h\nabla\phi_\alpha\cdot\nabla\phi_\beta\,dA\\ &\quad= \lambda_\alpha\int_{\mathcal{D}}\phi_\alpha\phi_\beta\,dA. \end{aligned} \tag{12.109}$$

Here, the divergence theorem has been applied. Hence,

$$\int_{\mathcal{D}}h\nabla\phi_\alpha\cdot\nabla\phi_\beta\,dA = \lambda_\alpha\int_{\mathcal{D}}\phi_\alpha\phi_\beta\,dA \tag{12.110}$$

and by interchanging the roles of α and β

$$\int_{\mathcal{D}}h\nabla\phi_\beta\cdot\nabla\phi_\alpha\,dA = \lambda_\beta\int_{\mathcal{D}}\phi_\beta\phi_\alpha\,dA \tag{12.111}$$

[12] This means that any two functions ϕ_α, ϕ_β or ψ_α, ψ_β are orthogonal but not ϕ_α with ψ_β.

Subtracting (12.111) from (12.110) yields

$$0 = (\lambda_\alpha - \lambda_\beta) \int_{\mathcal{D}} \phi_\alpha \phi_\beta \, dA \qquad \forall\ \alpha, \beta. \tag{12.112}$$

For different eigenvalues, $\lambda_\alpha \neq \lambda_\beta$, if $\alpha \neq \beta$, this implies $\int_{\mathcal{D}} \phi_\alpha \phi_\beta \, dA = 0$ proving orthogonality of the function set $\{\phi_\alpha\}$. An analogous proof can also be established for the functions $\{\psi_\alpha\}$. The analogous relation to (12.110) is

$$\begin{aligned} \int_{\mathcal{D}} h^{-1} \nabla \psi_\alpha \cdot \nabla \psi_\beta \, dA &= \int_{\mathcal{D}} h^{-1} (\hat{\mathbf{k}} \times \nabla \psi_\alpha) \cdot (\hat{\mathbf{k}} \times \nabla \psi_\beta) dA \\ &= \mu_\alpha \int_{\mathcal{D}} \psi_\alpha \psi_\beta \, dA. \end{aligned} \tag{12.113}$$

Writing this for α and β interchanged, we conclude as above, if $\mu_\alpha \neq \mu_\beta$, $\alpha \neq \beta$, that $\int_D \psi_\alpha \psi_\beta \, dA = 0$, proving orthogonality of the function set $\{\psi_\alpha\}$. Alternatively, relations (12.111) and (12.113), combined with (12.108), yield

$$\begin{aligned} \int_{\mathcal{D}} h \mathbf{v}_\alpha^\phi \cdot \mathbf{v}_\beta^\phi \, dA &= \lambda_\alpha \int_{\mathcal{D}} \phi_\alpha \phi_\beta \, dA = c^2 A \delta_{\alpha\beta}, \\ \int_{\mathcal{D}} h \mathbf{v}_\alpha^\psi \cdot \mathbf{v}_\beta^\psi \, dA &= \mu_\alpha \int_{\mathcal{D}} \psi_\alpha \psi_\beta \, dA = c^2 A \delta_{\alpha\beta}, \end{aligned} \tag{12.114}$$

in which $c^2 = g\bar{H}$, A is the area of $\mathcal{D}$ and $\delta_{\alpha\beta} = 1$, if $\alpha = \beta$ and $\delta_{\alpha\beta} = 0$, if $\alpha \neq \beta$. The expressions on the far right of (12.114) are the normalization conditions for the functions ϕ_α, ψ_α or $\mathbf{v}_\alpha^\phi$, $\mathbf{v}_\alpha^\psi$, $\alpha = 1, 2, \ldots, \infty$. Note that the construction of the function sets $\{\phi_\alpha\}$, $\{\psi_\alpha\}$ or $\{\mathbf{v}_\alpha^\phi\}$, $\{\mathbf{v}_\alpha^\psi\}$ is all based on the solution of the time-independent self-adjoint boundary value problems (12.106) and (12.107); thus, these functions can be determined prior to the solution of the dynamical problem (12.100) and (12.101). In a first step towards that purpose, we now proceed to express $\mathbf{v}^\phi$, $\mathbf{v}^\psi$ in terms of $\{\mathbf{v}_\alpha^\phi\}$, $\{\mathbf{v}_\alpha^\psi\}$. Using the ansatz

$$(\mathbf{v}^\phi, \mathbf{v}^\psi) = \sum_{\alpha=1}^{\infty} (p_\alpha \mathbf{v}_\alpha^\phi, q_\alpha \mathbf{v}_\alpha^\psi) \tag{12.115}$$

it is easily shown with the aid of (12.114) that

$$\begin{aligned} p_\alpha &= \frac{1}{c^2 A} \int_{\mathcal{D}} h \mathbf{v}_\alpha^\phi \cdot \mathbf{v}^\phi \, dA \overset{!}{=} \frac{1}{c^2 A} \int_{\mathcal{D}} h \mathbf{v}_\alpha^\phi \cdot \mathbf{v} \, dA, \\ q_\alpha &= \frac{1}{c^2 A} \int_{\mathcal{D}} h \mathbf{v}_\alpha^\psi \cdot \mathbf{v}^\psi \, dA \overset{!}{=} \frac{1}{c^2 A} = \int_{\mathcal{D}} h \mathbf{v}_\alpha^\psi \cdot \mathbf{v} \, dA. \end{aligned} \tag{12.116}$$

We remark that p_α and q_α are time dependent, since $\mathbf{v}^\phi$ and $\mathbf{v}^\psi$ are time dependent.

Having obtained orthogonal bases for $\mathbf{v}^\phi$ and $\mathbf{v}^\psi$, we must now establish a basis for the height field ζ. It follows from the mass balance equation $(12.100)_1$ that ζ can be expressed in terms of $\{\phi_\alpha\}$ alone, since the functions $\mathbf{v}_\alpha^\psi$ are solenoidal. Therefore, we write

$$\zeta_\alpha = \gamma_\alpha \phi_\alpha \tag{12.117}$$

and determine the normalization by the condition that

$$\underbrace{\int_{\mathcal{D}} \zeta_\alpha \zeta_\beta \, dA}_{\bar{H}^2 A \delta_{\alpha\beta}} = \gamma_\alpha \gamma_\beta \int_{\mathcal{D}} \phi_\alpha \phi_\beta \, dA \overset{(12.114)_1}{=} \gamma_\alpha \gamma_\beta c^2 A \lambda_\alpha^{-1} \delta_{\alpha\beta}, \tag{12.118}$$

where the choice $\bar{H}^2 A \delta_{\alpha\beta}$ for the integration of the left-hand side is based only on reasons of dimensionality. This implies

$$\gamma_\alpha = \bar{H} \sqrt{\lambda_\alpha} c^{-1}, \qquad \zeta_\alpha = \bar{H} \sqrt{\lambda_\alpha} c^{-1} \phi_\alpha, \tag{12.119}$$

$$\int_{\mathcal{D}} \zeta_\alpha \zeta_\beta \, dA = \bar{H}^2 A \delta_{\alpha\beta}. \tag{12.120}$$

With this normalization the expansion

$$\zeta = \sum_{\alpha=1}^{\infty} r_\alpha \zeta_\alpha \tag{12.121}$$

and relation (12.120) imply

$$r_\alpha \equiv \frac{1}{\bar{H}^2 A} \int_{\mathcal{D}} \zeta_\alpha \zeta \, dA, \tag{12.122}$$

which is dimensionless.

Associated with the expansions (12.115) and (12.120) are the so-called Parceval relations

$$\begin{aligned} K^\phi &= \frac{1}{2} \rho \bar{H} \int_{\mathcal{D}} h \mathbf{v}^\phi \cdot \mathbf{v}^\phi \, dA \\ &= \frac{1}{2} \rho \bar{H} \int_{\mathcal{D}} h \left(\sum_\alpha p_\alpha \mathbf{v}_\alpha^\phi \right) \cdot \left(\sum_\beta p_\beta \mathbf{v}_\beta^\phi \right) dA \end{aligned}$$

$$= \frac{1}{2}\rho\bar{H}\sum_{\alpha,\beta} p_\alpha p_\beta \underbrace{\int_{\mathcal{D}} h\mathbf{v}_\alpha^\phi \cdot \mathbf{v}_\beta^\phi dA}_{c^2 A\delta_{\alpha\beta}\ (12.114)_1}$$

$$= \frac{1}{2}\underbrace{(\rho\bar{H}A)}_{M} c^2 \sum_\alpha p_\alpha^2 = \frac{1}{2}Mc^2\sum_\alpha p_\alpha^2, \tag{12.123}$$

$$K^\psi = \frac{1}{2}\rho\bar{H}\int_{\mathcal{D}} h\mathbf{v}^\psi \cdot \mathbf{v}^\psi dA$$

$$= \frac{1}{2}\rho\bar{H}\int_{\mathcal{D}} h\left(\sum_\alpha q_\alpha \mathbf{v}_\alpha^\psi\right)\cdot\left(\sum_\beta q_\beta \mathbf{v}_\beta^\psi\right) dA$$

$$= \frac{1}{2}\rho\bar{H}\sum_{\alpha,\beta} q_\alpha q_\beta \underbrace{\int_{\mathcal{D}} h\mathbf{v}_\alpha^\psi \cdot \mathbf{v}_\beta^\psi dA}_{c^2 A\delta_{\alpha\beta}\ (12.114)_2}$$

$$= \frac{1}{2}\underbrace{(\rho\bar{H}A)}_{M} c^2 \sum_\alpha q_\alpha^2 = \frac{1}{2}Mc^2\sum_\alpha q_\alpha^2, \tag{12.124}$$

$$P = \frac{1}{2}\rho g\int_{\mathcal{D}} \zeta^2 dA = \frac{1}{2}\rho g\int_{\mathcal{D}}\sum_{\alpha,\beta} r_\alpha r_\beta \zeta_\alpha\zeta_\beta dA$$

$$= \frac{1}{2}\rho g\sum_{\alpha,\beta} r_\alpha r_\beta \underbrace{\int_{\mathcal{D}} \zeta_\alpha\zeta_\beta dA}_{\bar{H}^2 A\delta_{\alpha\beta}\ (12.120)}$$

$$= \frac{1}{2}\underbrace{(\rho\bar{H}A)}_{M}\underbrace{(g\bar{H})}_{c^2}\sum_\alpha r_\alpha^2 = \frac{1}{2}Mc^2\sum_\alpha r_\alpha^2. \tag{12.125}$$

Here, K^ϕ and K^ψ are the kinetic energies of the irrotational and solenoidal motion fields and P is the (gravitational) potential energy. Evidently,

$$K^\phi + K^\psi + P = \frac{1}{2}Mc^2\sum_\alpha\left(p_\alpha^2 + q_\alpha^2 + r_\alpha^2\right) \tag{12.126}$$

is the total energy.

Having established spectral representations of $\mathbf{v}$ and ζ in terms of p_α, q_α, and r_α ($\alpha = 1, 2, \ldots, \infty$), we must now explore (12.100) to find a system of ordinary differential equations for these coefficients. First, we differentiate p_α, q_α as given in (12.116) and r_α in (12.122) with respect to time. Since the limits of integrations (the basin boundaries) are assumed independent of time, and since the characteristic functions $\mathbf{v}_\alpha^\phi$, $\mathbf{v}_\alpha^\psi$, ζ_α are also time independent, the result of this differentiation is merely to introduce $\partial\mathbf{v}/\partial t$ in place of $\mathbf{v}$ in (12.116) and $\partial\zeta/\partial t$ in place of ζ in (12.122):

$$\left.\begin{aligned} \frac{dp_\alpha}{dt} &= \frac{1}{c^2 A}\int_{\mathcal{D}} h\mathbf{v}_\alpha^\phi \cdot \frac{\partial \mathbf{v}}{\partial t} dA, \\ \frac{dq_\alpha}{dt} &= \frac{1}{c^2 A}\int_{\mathcal{D}} h\mathbf{v}_\alpha^\psi \cdot \frac{\partial \mathbf{v}}{\partial t} dA, \\ \frac{dr_\alpha}{d} &= \frac{1}{\bar{H}^2 A}\int_{\mathcal{D}} \zeta_\alpha \frac{\partial \zeta}{\partial t} dA. \end{aligned}\right\} \tag{12.127}$$

In these relations, $\partial\mathbf{v}/\partial t$, $\partial\zeta/\partial t$ are next eliminated with the aid of (12.100). In doing this and making use of (12.106)–(12.108), (12.115), (12.116), and $(12.119)_2$, the resulting equations can be put into the form

$$\left.\begin{aligned} \frac{dp_\alpha}{dt} &= \nu_\alpha \frac{d^2 r_\alpha}{dt} + f\sum_\beta \left(a_{\alpha\beta} p_\beta + b_{\alpha\beta} q_\beta\right), \\ \frac{dq_\alpha}{dt} &= f\sum_\beta \left(c_{\alpha\beta} p_\beta + \underbrace{d_{\alpha\beta}}_{0} q_\beta\right), \\ \frac{dr_\alpha}{dt} &= -\nu_\alpha p_\alpha, \end{aligned}\right\} \tag{12.128}$$

in which the constant coefficients $\nu_\alpha, a_{\alpha\beta}, \ldots, d_{\alpha\beta}$ are defined as

$$\left.\begin{aligned} \nu_\alpha &:= \sqrt{c^2\lambda_\alpha}, \\ a_{\alpha\beta} &:= \langle \mathbf{v}_\alpha^\phi, -\hat{\mathbf{k}}\times\mathbf{v}_\beta^\phi\rangle, \quad b_{\alpha\beta} := \langle \mathbf{v}_\alpha^\phi, -\hat{\mathbf{k}}\times\mathbf{v}_\beta^\psi\rangle, \\ c_{\alpha\beta} &:= \langle \mathbf{v}_\alpha^\psi, -\hat{\mathbf{k}}\times\mathbf{v}_\beta^\phi\rangle, \quad d_{\alpha\beta} := \langle \mathbf{v}_\alpha^\psi, -\hat{\mathbf{k}}\times\mathbf{v}_\beta^\psi\rangle, \end{aligned}\right\} \tag{12.129}$$

where the inner product $\langle \mathbf{f}, \mathbf{g}\rangle$ is defined as

$$\langle \mathbf{f}, \mathbf{g}\rangle := \frac{1}{c^2 A}\int_{\mathcal{D}} h\mathbf{f}\cdot\mathbf{g} dA. \tag{12.130}$$

Note that the coupling coefficients depend only on the basin geometry and the functions ϕ_α, ψ_α which are also known, if the geometry is prescribed. Moreover, it follows from the definitions (12.129), (12.130) that

$$a_{\alpha\beta} = -a_{\beta\alpha}, \quad b_{\alpha\beta} = -c_{\beta\alpha}, \quad d_{\alpha\beta} = 0. \tag{12.131}$$

It is apparent from (12.128) that ν_α is the frequency of the normal modes in the zero-rotation case ($f = 0$). Rotation introduces a coupling between the p_α's and q_α's so that, when $f \neq 0$, the normal modes can only be built through linear combinations of $p_\alpha, q_\alpha, r_\alpha$. This spectral-type solution method is due to Proudman [33].

The ordinary differential equations (12.128) are homogeneous and linear with constant coefficients. They can, in principle, be solved by assuming solutions of the form

$$(p_\alpha, q_\alpha, r_\alpha) = (\check{p}_\alpha, \check{q}_\alpha, \check{r}_\alpha)\exp(-i\omega t) \tag{12.132}$$

and truncating the number of characteristic functions at $\alpha = M_p + M_q + M_\zeta$. Substituting (12.132) into (12.128) yields a matrix equation of the form

$$M_{\alpha\beta}(\omega)x_\beta = 0 \qquad \alpha, \beta = 1, 2, M_p + M_q + M_\zeta, \tag{12.133}$$

with a frequency dependent square matrix $\mathbf{M}$ of dimension $(M_p + M_q + M_\zeta) \times (M_p + M_q + M_\zeta)$ and vector $\mathbf{x}$, collecting all amplitudes $(\check{p}_\alpha, \check{q}_\alpha, \check{r}_\alpha)$. Admissible values of ω then follow from the solvability condition

$$\det \mathbf{M}(\omega) = 0. \tag{12.134}$$

This is essentially the procedure that was taken by Proudman [33] to determine the eigenfrequencies of the gravity induced rotational modes in a cylindrical basin with constant and parabolic bottom. Rao [40] employed it to find the oscillations of the fluid in a rotating rectangle of constant depth and free surface, whilst Maas [21] did the same for the inertial waves proper. The corresponding computations are not easy and still rather involved. The reader is asked to consult the literature.

The method is ideally suited to lake geometries and bathymetries of regular shape. In principle, however, it is applicable to any given basic geometry. Each lake then will give rise to its own function sets $\{\phi_\alpha\}$ and $\{\psi_\alpha\}$. These can be determined once and for all. When this is done, the solution procedure is to solve a system of ordinary differential equations in time. To our knowledge this has so far not been tried with real lakes.

References

1. Bjerknes, V., Bjerknes, J., Solberg, H. and Bergeron, T.T.: *Physikalische Hydrodynamik*, Springer, Berlin, etc. (1933)
2. Brown, P.J.: Kelvin wave reflection in a semi-infinite canal. *J. Mar. Res.*, **31**, 1–10 (1973)

3. Bryan, G.: The waves on a rotating liquid spheroid of finite ellipticity. *Phil. Trans. Royal Soc. Lond.*, **180**, 187–219 (1889)
4. Cartwright, D.: *Tides, a Scientific History*. Cambridge University Press, Cambridge (1999)
5. Chapman, D.: On the failure of Laplace's tidal equations to model sub-inertial motions at a discontinuity in depth. *Dyn. Atmos. Oceans*, **7**, 1–16 (1982)
6. Chapman, D. and Hendershott, M.: Shelf wave dispersion in a geophysical ocean. *Dyn Atmos. Oceans*, **7**, 17–31 (1982)
7. Corkan, R.H. and Doodson, A.T.: Free oscillations in a rotating square sea. *Proc. Roy. Soc. London A*, **21**, 147 (1952)
8. Defant, A.: *Gezeitenprobleme des Meeres in Landnähe*. (published in "Probleme der kosmischen Physik", Vol. 6) Hamburg, Henri Grand, p 80 (1925)
9. Defant, F.: Theorie der Seiches des Michigansees und ihre Abwandlung durch Wirkung der Corioliskraft. *Arch. Met. Geophys. Biokl.*, **A 6**, 218–241 (1953)
10. Goldsbrough, G.R.: The tidal oscillations in rectangular basins. *Proc. Roy. Soc. London A*, **132**, 689 (1931)
11. Jeffreys, H.: The free oscillations of water in an elliptical lake. *Proc. Lond. Math. Soc.*, **23**, 455–476 (1925)
12. Kelvin, L. (William Thomson): On the gravitational oscillations of rotating water. *Proc. Roy. Soc. Edinburgh*, **10**, 92–100, (1979); reprinted *Phil. Mag.*, **10**, 109–116 (1880)
13. Kelvin, L.: Vibrations of a columnar vortex. *Philos. Mag.*, **10**, 155–168 (1880)
14. Krauss, W.: *Interne Wellen*. Gebrüder Bornträger, Berlin, Nikolassee (1966)
15. Krauss, W.: *Methods and Results of Theoretical Oceanography I, Dynamics of the homogeneous and the quasi-homogeneous Ocean*. Gebr. Bornträger (1973)
16. Lamb, H.: *Hydrodynamics*. Cambridge University Press (1924)
17. Lamb, H.: *Hydrodynamics*. 6th edition, Cambridge University Press (1932)
18. LeBlond, P.H. and Mysak, L. A.: *Waves in the Ocean* Elsevier Sci. Publ, Amsterdam 602 p.(1978)
19. Lifschitz, A. and Fabijonas, B.: A new class of instabilities of rotating fluids. *Phys. Fluids*, **8**, 2239–2241 (1996)
20. Lighthill, S.M.J.: Dynamics of rotating fluids: a survey. *J. Fluid Mech.*, **26**, 411–431 (1966)
21. Maas, L.R.M.: On the amphidromic structure of inertial waves in a rectangular parallelepiped. *Fluid Dynamics Research*, **33**, 373–401 (2003)
22. Mortimer, C. H.: Frontiers in physical limnology with particular reference to long waves in rotating basins. *Proc. 5th Conf. Great Lakes Res., Great Lakes Res. Div. Univ. Michigan*, **9**, 9–42 (1963)
23. Mortimer, C. H.: *Large scale oscillatory motions and seasonal temperature changes in Lake Michigan and Lake Ontario* Special Report No 12, **Part I**, 11 p.: Text, **Part II**, 106 p.: Illustrations, Center for Great Lakes Studies, The University of Wisconsin-Milwaukee (1971)
24. Mortimer, C. H.: Lake Hydrodynamics *Mitt. Int. Ver. Theor. Angew. Limnol.*, **20**, 124–197 (1974)
25. Mortimer, C. H.: Substantive corrections to SIL Communications (IVL Mitteilungen) Nrs 6 and 20. *Mitt. Int. Ver. Theor. Angew. Limnol.*, **19**, 60–72 (1975)
26. Mortimer, C. H.: *Internal waves observed in Lake Ontario during the International Field Year for the Great Lakes (IFYGL), 1977: descriptive theory and preliminary interpretations of near-inertial oscillations in terms of linear channel models*. Special Report no 32, Center for Great Lakes Studies, The University of Wisconsin-Milwaukee, 122 p. (1977)
27. Mortimer, C. H.: *Internal motion and related internal waves in Lake Michigan and Lake Ontario as responses to impulsive wind stresses*. Special Report no 37, Center for Great Lakes Studies, The University of Wisconsin-Milwaukee, 192 p. (1980)
28. Platzman, G. and Rao, D.B.: The free oscillations of Lake Erie. In: *Studies on Oceanography* (Hidaka Volume) (ed. K. Yoshida), 359–382, University of Washington Press (1964)
29. Platzman, G. : Ocean Tides and Related Waves *Amer. Math. Soc. Lectures in Applied Mathematics*, **14**, 239–291 (1971)
30. Poincaré, H.: Sur l'équilibre d'une masse de fluide animee d'un movement de rotation. *Acta Mathematica*, VII, 259–380 (1885)

31. Poincaré, H.: Sur la precession des corps deformables. *Bull. Astronom.*, **27**, 321 (1910)
32. Prandle, D.: The vertical structure of tidal currents. *Geophys. Astrophys. Fluid Dyn.*, **22**, 29–49 (1982)
33. Proudman, J.: On the dynamical theory of tides. Part (ii): flat seas. *Proc. London Math. Soc.*, 2nd Series, **18**, 21–50 (1916)
34. Proudman, J.: Note on the free tidal oscillations of a sea with slow rotation. *Proc. Lond. Math. Soc.*, (2nd series), **35**, 75 (1933)
35. Raggio, G. and Hutter, K.: An extended channel model for the prediction of motion in elongated homogeneous lakes. Part 1. Theoretical introduction. *J. Fluid Mech.*, **121**, 231-255 (1982)
36. Raggio, G. and Hutter, K.: An extended channel model for the prediction of motion in elongated homogeneous lakes. Part 2. First order model applied to ideal geometry: rectangular basins with flat bottom. *J. Fluid Mech.*, **121**, 257-281 (1982)
37. Raggio, G. and Hutter, K.: An extended channel model for the prediction of motion in elongated homogeneous lakes. Part 3. Free oscillations in natural basins *J. Fluid Mech.*, **121**, 283-299 (1982)
38. Hutter, K. and Raggio, G.: A Chrystal-model describing gravitational barotropic motion in elongated lakes *Arch. Met. Geophys. Biokl.*, **Ser A, 31**, 361-378 (1982)
39. Rao, D.B.: *Free gravitational oscillations in rotating rectangular basins*. Ph.D Thesis, Department of Geophysical Sciences, The University of Chicago (1965)
40. Rao, D.B.: Free gravitational oscillations in rotating rectangular basins. *J. Fluid Mech.*, **25**, 523–555 (1966)
41. Rayleigh, L.: On the vibrations of a rectangular sheet of rotating liquid. *Phil. Mag.*, **5**, 297 (1903)
42. Rayleigh, L.: Notes concerning tidal oscillations upon a rotating globe. *Proc. Roy. Soc. A*, **82**, 448 (1909)
43. Rieutord, M., Georgeot, B. and Valdettaro, L.: Wave attractors in rotating fluids: a paradigm for ill-posed Cauchy problems. *Phys. Rev. Lett.*, **85**, 4277–4280, (2000)
44. Solberg, H.: Über die freien Schwingungen einer homogenen Flüssigkeitsschicht auf der rotierenden Erde. *I. Astophys. Norv.*, **1**, 237–340 (1936)
45. Taylor, G.I.: Tidal oscillations in gulfs and basins. *Proc. London Math. Soc.*, Series 2, XX, 148–181 (1920)
46. Van Danzig, D. and Lauwerier, H.A.: The North Sea Problem. IV. Free oscillations of a rotating rectangular sea. *Proc. K. ned. Akad. Wet.* (Series A), **63**, 339 (1960)
47. Whewell: Essay towards a first approximation to a map of co-tidal lines. *Phil. Trans. Royal Soc. London*, **123**, 147–236 (1833)

http://www.springer.com/978-3-642-19111-4

Physics of Lakes
Volume 2: Lakes as Oscillators
Hutter, K.; Wang, Y.; Chubarenko, I.P.
2011, LXVIII, 646 p., Hardcover
ISBN: 978-3-642-19111-4